A&A 653, A11 (2021)
https://doi.org/10.1051/0004-6361/202141012

Astronomy & Astrophysics

MaNGA galaxies with off-centered spots of enhanced gas velocity dispersion

L. S. Pilyugin[1], B. Cedrés[2,3], I. A. Zinchenko[4,1], A. M. Pérez Garcia[5,6], M. A. Lara-López[7], J. Nadolny[2,3], Y. A. Nefedyev[8], M. González-Otero[2,3], J. M. Vílchez[9], S. Duarte Puertas[10], and R. Navarro Martinez[2,3]

[1] Main Astronomical Observatory, National Academy of Sciences of Ukraine, 27 Akademika Zabolotnoho St, 03680 Kiev, Ukraine
e-mail: pilyugin@MAO.Kiev.UA
[2] Instituto de Astrofísica de Canarias (IAC), 38200 La Laguna, Tenerife, Spain
[3] Departamento de Astrofísica, Universidad de la Laguna (ULL), 38205 La Laguna, Tenerife, Spain
[4] Faculty of Physics, Ludwig-Maximilians-Universität, Scheinerstr. 1, 81679 Munich, Germany
[5] Centro de Astrobiología (CSIC/INTA), 28692 ESAC Campus, Villanueva de la Cañada, Madrid, Spain
[6] Asociación Astrofísica para la Promoción de la Investigación, Instrumentación y su Desarrollo, ASPID, 38205 La Laguna, Tenerife, Spain
[7] Armagh Observatory and Planetarium, College Hill, Armagh BT61 9DG, Northern Ireland, UK
[8] Kazan Federal University, 18 Kremlyovskaya St., 420008 Kazan, Russian Federation
[9] Instituto de Astrofísica de Andalucía, CSIC, Apdo 3004, 18080 Granada, Spain
[10] Département de Physique, de Génie Physique et d'Optique, Université Laval, and Centre de Recherche en Astrophysique du Québec (CRAQ), Québec, QC G1V 0A6, Canada

Received 7 April 2021 / Accepted 21 June 2021

ABSTRACT

Off-centered spots of the enhanced gas velocity dispersion, σ, are revealed in some galaxies from the Mapping Nearby Galaxies at Apache Point Observatory survey (MaNGA). Aiming to clarify the origin of the spots of enhanced σ, we examine the distributions of the surface brightness, the line-of-sight velocity, the oxygen abundance, the gas velocity dispersion, and the Baldwin-Phillips-Terlevich spaxel classification in seven galaxies. We find that the enhanced σ spots in six galaxies can be attributed to a (minor) interaction with a satellite. Three galaxies in our sample have a very close satellite (the separation in the sky plane is comparable to the optical radius of the galaxy). The spots of enhanced σ in those galaxies are located at the edge of the galaxy close to the satellite. The spots of enhanced σ in three other galaxies are related to bright spots in the photometric B band within the galaxy, which can be due to the projection of a satellite in the line of sight of the galaxy. The oxygen abundances in the spots in these three galaxies are reduced. This suggests that the low-metallicity gas from the satellite is mixed with the interstellar medium of the disk, that is, the gas exchange between the galaxy and its satellite takes place. The spectra of the spaxels within a spot are usually H II-region-like, suggesting that the interaction (gas infall) in those galaxies does not result in appreciable shocks. In contrast, the spot of the enhanced σ in the galaxy M-8716-12703 is associated with an off-centered active galactic nucleus-like radiation distribution. One can suggest that the spot of the enhanced σ in the M-8716-12703 galaxy is different in origin, or that the characteristics of gas infall in this case differs from that in other galaxies.

Key words. galaxies: general

1. Introduction

The gas velocity dispersion of nearby disk galaxies traced by ionized gas is higher than the expected dispersion due to thermal motion alone (Epinat et al. 2010; Varidel et al. 2020; Bacchini et al. 2020), and there is a trend of increasing gas velocity dispersion with increasing redshift (Johnson et al. 2018; Übler et al. 2019; Hung et al. 2019). Although several mechanisms for the enhancement of the gas velocity dispersion in disk galaxies (including feedback from star formation activity and a galaxy interaction and merger or intergalactic gas acretion) have been considered; the drivers responsible for the enhancement of the gas velocity dispersion are still debated (Stilp et al. 2013; Zhou et al. 2017; Hung et al. 2019; Kohandel et al. 2020; Hunter et al. 2021, and references therein).

Numerical simulations predict that the enhancement of the gas velocity dispersion in the disk can be caused by feedback from star formation activity, including supernovae and winds from stars (e.g., Dib et al. 2006). The validity of the predicted relationship between the velocity dispersion of the gas and the star formation rate (or supernova rate) has been tested through the comparison with observations. However, the available observations have not decisively identified the main driver of the gas velocity dispersion. Indeed, Lehnert et al. (2013) and Bacchini et al. (2020) conclude that supernovae alone can sustain gas turbulence in galaxies and that there is essentially no need for any further source of energy. On the contrary, Krumholz et al. (2018) and Varidel et al. (2020) found that the radial gas transport should be added to star formation feedback in order to explain the observed gas velocity dispersion in galaxies.

The enhancement of the gas velocity dispersion in the disk can be caused by interaction and merger or accretion (Klessen & Hennebelle 2010; Bournaud et al. 2011). Simulations of interactions and mergers of galaxies are the topic of many works (Walker et al. 1996; Naab & Burkert 2003; Bournaud et al. 2004; Springel & Hernquist 2005; Robertson et al. 2006;

Governato et al. 2007; Lotz et al. 2008; Hopkins et al. 2009a,b; Zinchenko et al. 2015; Rodriguez-Gomez et al. 2017, among many others). It is established that the observed properties of the interaction or merger remnants depend on the characteristics of the progenitors, the geometry of the collision, and the merger stage. The properties of the merger remnant depend strongly on the mass ratio of the progenitors. Major galaxy mergers with mass ratios in the range 1:1–3:1 lead to the formation of boxy or disky elliptical galaxies, mergers with mass ratios in the intermediate range 4:1–10:1 result in peculiar galaxies with disk-type morphologies, but kinematics closer to that of elliptical systems. On the other hand, minor mergers with mass ratios below 10:1 result in disturbed spiral galaxies (Bournaud et al. 2004). The difference between minor merger and accretion is blured (Hopkins et al. 2009b). The properties of the merger remnant are also determined by the gas fraction of the progenitors. When the gas fraction of the progenitors is low then the remnants structurally and kinematically resemble elliptical galaxies. If the progenitor galaxies are gas-rich then a prominent preexisting disk can survive, that is, both major and minor mergers can produce a disk-dominated galaxy. Rodriguez-Gomez et al. (2017) considered the influence of mergers in the galaxy morphology using the Illustris simulations. They found that mergers play a dominant role in shaping the morphology of massive galaxies, while mergers do not seem to play any significant role in determining the morphology of galaxies with masses below $\sim 10^{11}\,M_{\odot}$.

This is the third paper of series devoted to the investigation of the distribution of the gas velocity dispersion σ in star-forming (SF) galaxies from the Mapping Nearby Galaxies at Apache Point Observatory (MaNGA) survey (Bundy et al. 2015; Albareti et al. 2017). In the first paper, we considered the circumnuclear regions of 161 galaxies from the Sloan Digital Sky Survey Data Release 15 (SDSS DR15) MaNGA survey (Pilyugin et al. 2020a). The spaxel spectra were classified as active galactic nucleus-like (AGN-like), H II-region-like (or SF-like), and intermediate (INT) spectra according to their positions in the Baldwin-Phillips-Terlevich (BPT, Baldwin et al. 1981) diagnostic diagram. There are four configurations in the type of radiation of the circumnuclear regions: (1) AGN, the innermost region is AGN-like radiation and is surrounded by a ring of radiation of the intermediate type; (2) INT, the central area of radiation is of the intermediate type; (3) SF+INT, the inner region is H II-like radiation and is surrounded by a ring of radiation of the intermediate type; and (4) SF, the central area is H II-like radiation only. We found that the AGN-like and INT radiation in the circumnuclear region is accompanied by an enhancement in the gas velocity dispersion σ, in the sense that the gas velocity dispersion in a galaxy decreases with galactocentric distance up to some radius and remains approximately constant beyond this radius. The radius of the area of the AGN-like and INT radiation (radius of influence of the AGN on the radiation) is similar to the radius of the area with enhanced gas velocity dispersion, and the central gas velocity dispersion σ_c correlates with the luminosity of the AGN+INT area. This suggests that the enhancement of the gas velocity dispersion at the center of a galaxy can be attributed to the AGN activity.

In the second paper, the distribution of the gas velocity dispersion σ across the images of 1146 MaNGA galaxies beyond the centers is analyzed (Pilyugin et al. 2021). We find that there are two types of distribution of the gas velocity dispersion across the images of galaxies: (i) the distributions of 909 galaxies show a radial symmetry with or without a σ enhancement at the center (R distribution) and (ii) distributions with a band of enhanced σ along the minor axis in the images of 159 galaxies with or without a σ enhancement at the center (B distribution). The σ distribution across the images of 78 galaxies cannot be reliable classified. We find that the median value of the gas velocity dispersion σ_m in galaxies with B distribution is higher by around $5\,km\,s^{-1}$, on average, than that of galaxies with R distribution. The optical radius R_{25} of galaxies with B distribution is lower by around 0.1,dex, on average, than that of galaxies with similar masses with R distribution. Thus the properties of a galaxy are related to the type of distribution of the gas velocity dispersion σ across its image. This suggests that the presence of the band of the enhanced gas velocity dispersion can be an indicator of a specific evolution (or a specific stage in the evolution) of a galaxy.

We find that there are off-centered spots of enhanced gas velocity dispersion σ in some MaNGA galaxies. The global distribution of the gas velocity dispersion σ across the image of the galaxy is more or less regular (with or without the σ enhancement at the center and with or without the band of enhanced σ along the minor axis), and values of the gas velocity dispersion in the spot show an evident deviation from the global distribution. To examine the origin of the enhanced σ spots, we produce and analyze maps of the surface brightness, line-of-sight velocity, oxygen abundance, gas velocity dispersion, and BPT spaxel classification in seven MaNGA galaxies that show off-centered spots of enhanced gas velocity dispersion. The parameters of emission lines in each spaxel spectrum are estimated using a single Gaussian fit to the line profiles. The sigma of the best-fit Gaussian of the Hα line is converted into the gas velocity dispersion σ.

This paper is organized as follows. The data are described in Sect. 2. In Sect. 3, the distributions of the gas velocity dispersion and other characteristics in the MaNGA galaxies are constructed and the comments on individual galaxies are given. In Sect. 4 a discussion is given, and Sect. 5 provides a brief summary.

2. Data

The publicly available spectroscopic observations from the Sloan Digital Sky Survey Data Release 15 (SDSS DR15) MaNGA survey (Bundy et al. 2015; Albareti et al. 2017) are at the base of this investigation. The same data was also used in our previous studies (Pilyugin et al. 2020a, 2021), and the data reduction is described in Zinchenko et al. (2016) and Sakhibov et al. (2018). Briefly, we used LOGCUBE datacubes, which have logarithmic wavelength sampling. The stellar radiation contribution is approximated using the public version of the STARLIGHT code (Cid et al. 2005; Mateus et al. 2006; Asari et al. 2007), which was adapted for execution in the NorduGrid Advanced Resource Connector (ARC)[1] environment of the Ukrainian National Grid. We use a sample of stellar population (SSP) spectra from the evolutionary synthesis models of Bruzual & Charlot (2003). The correction for reddening is performed using the curve from Cardelli et al. (1989) with R_V = 3.1. The gaseous spectrum is obtained by subtracting the derived stellar radiation contribution from the observed spectrum.

The emission line profiles in each spaxel spectrum were fitted by single Gaussians using our emission line fitting code ELF3D. The code is based on the iminuit library. Since the applied fitting scheme is sensitive to the choice of the initial parameters, we implemented a Monte Carlo (MC) approach for choosing the initial parameters of the fit, which significantly increased the robustness of the fitting. ELF3D allows to fit lines

[1] http://www.nordugrid.org/

independently or in groups where central wavelengths and/or widths of profiles can be tied. In this work we tied the center and width of the following lines doublets [O II]$\lambda\lambda$3727,3729, [O III]$\lambda\lambda$4959,5007, and [N II]$\lambda\lambda$6548,6584. Also, the lines center of the [N II]$\lambda\lambda$6548,6584 doublet have been tied to Hα as they have been fitted in the same group.

The estimated emission line parameters are the central wavelength λ_0, the sigma σ, and the flux F. For each spectrum, the [O II]$\lambda\lambda$3727,3729, Hβ, [O III]λ5007, Hα, and [N II]λ6584 emission lines were measured. In the construction of each particular map, only those spaxel spectra where the concerned lines were measured with a signal-to-noise ratio $S/N > 3$ were used. In some spectra, the strong Hα line is measured with $S/N > 3$ while the weak lines (e.g., [N II]λ6584 line) are measured with $S/N < 3$. Therefore the different maps for a given galaxy can contain different numbers of the spaxels. The central wavelength of the Hα line was converted into the line-of-sight velocity $V_{\rm los}$, and the sigma of the best-fit Gaussian $\sigma_{\rm H\alpha}$ was converted into the observed gas velocity dispersion $\sigma_{\rm obs}$. Since the values of the observed (non-corrected-for instrumental profile) gas velocity dispersion are used throughout the paper, we use the notation σ instead of $\sigma_{\rm obs}$.

The interstellar reddening is estimated through the comparison between the measured and the theoretical Hα/Hβ ratios using the reddening law from Cardelli et al. (1989) for $R_V = 3.1$. It was adopted $C_{\rm H\beta} = 0.47 A_V$ (Lee et al. 2005). We classify the excitation of the spaxel spectrum using its position on the standard diagnostic diagram of the [N II]λ6584/Hα versus the [O III]λ5007/Hβ line ratios suggested by Baldwin et al. (1981), which is known as the BPT classification diagram. As in our previous studies (Zinchenko et al. 2019; Pilyugin et al. 2020a,b, 2021), the spectra located to the left (below) the demarcation line from Kauffmann et al. (2003) are referred to as the SF-like or H II region-like spectra, those located to the right (above) the demarcation line from Kewley et al. (2001) are referred to as the AGN-like spectra, and the spectra located between those demarcation lines are the intermediate (INT) spectra.

The geometrical parameters of the galaxy needed to determine the galactocentric distances of the spaxels, are derived from the analysis of the observed velocity field in the standard way assuming that a galaxy is a symmetrically rotating disk (e.g., Warner et al. 1973; Begeman 1989; de Blok et al. 2008; Oh et al. 2018). The position of the kinematic center of the galaxy, the position angle of the major kinematic axis and the kinematic inclination angle are determined from the measured line-of-sight gas velocities (obtained from the Hα line) in the same way as in our previous papers (Pilyugin et al. 2019, 2020b; Zinchenko et al. 2019). Briefly, the observed line-of-sight velocities recorded on a set of pixel coordinates (1 pixel = 0.5 arcsec for MaNGA galaxies) are related to the kinematical parameters of the galaxy and its rotation curve. We divide the deprojected galaxy plane into rings with a width of one pixel. It is assumed that the rotation velocity is the same for all the spaxels within the ring. We adopt that the position angle of the major kinematic axis and the galaxy inclination angle are the same for all the rings. The coordinates of the rotation center of the galaxy, the position angle of the major kinematic axis, the galaxy inclination angle, and the rotation curve are determined through the best fit of the line-of-sight velocity field $V_{\rm los}$. We follow two steps for deriving the rotation curve and the geometrical parameters of each galaxy. In the first step, the values of the parameters are obtained for all the spaxels with measured $V_{\rm los}$. In the second step, we use an iterative procedure to determine the rotation curve and the geometrical parameters. At each step, points with large deviations from the rotation curve determined in the previous step are rejected, and new values of the geometrical parameters and the rotation curve are derived. The difference between the values of the spaxel velocity obtained from the measured wavelengths of the Hβ and Hα lines can be considered as some kind of estimation of the error in the spaxel line-of-sight velocity measurements in the MaNGA spectra. The mean value of the differences between the measured Hβ and Hα velocities in 46 350 spaxels in the MaNGA galaxies is $\sim$7 km s^{-1} (Pilyugin et al. 2019). The points with deviations larger than 21 km s^{-1} (three sigma) from the rotation curve determined in the previous step are rejected. The iteration is stopped when the absolute values of the difference of coordinates of the center obtained in successive steps is less than 0.1 pixels, the difference of position angle of the major axis and the inclination angle is smaller than 0.1°, and the rotation curves agree within 1 km s^{-1} (at each radius). A detailed discussion of the determination of coordinates of the rotation center, the inclination angle, the position angle of the major kinematic axis, and the rotation curve can be found in Pilyugin et al. (2019).

The surface brightness in the SDSS g and r bands for each spaxel was obtained from broadband SDSS images created from the data cube. The measured magnitudes are converted to B-band magnitudes and corrected for Galactic foreground extinction using the recalibrated A_V values from Schlafly & Finkbeiner (2011) as reported in the NASA/IPAC Extragalactic Database (NED)[2]. The observed surface-brightness profile is obtained using the geometrical parameters of the galaxy derived from the observed velocity field analysis (the position of the kinematic center of the galaxy, the position angle of the major kinematic axis and the kinematic inclination angle). The observed surface-brightness profile within a galaxy was fitted by a broken exponential profile for the disk and by a general Sérsic profile for the bulge (Pilyugin et al. 2014, 2017, 2018). The optical radius of the galaxy R_{25} was estimated using the obtained fit.

The distances to the galaxies were taken from NED. The NED distances use flow corrections for Virgo, the Great Attractor, and Shapley Supercluster infall (adopting a cosmological model with $H_0 = 73$ km s^{-1} Mpc^{-1}, $\Omega_{\rm m} = 0.27$, and $\Omega_\Lambda = 0.73$). We have chosen the spectroscopic $M_{\rm sp}$ masses of the SDSS and BOSS (BOSS stands for the Baryon Oscillation Spectroscopic Survey in SDSS-III, see Dawson et al. 2013). The spectroscopic masses are taken from the table STELLARMASSPCAWISCBC03, and were determined using the Wisconsin method (Chen et al. 2012) with the stellar population synthesis models from Bruzual & Charlot (2003).

The oxygen abundances were obtained through the three-dimensional R calibration (Pilyugin & Grebel 2016; Pilyugin et al. 2018). The [O II]$\lambda\lambda$3727,3729, Hβ, [O III]$\lambda\lambda$4959, 5007, and [N II]$\lambda\lambda$6548,6584 emission lines are used for oxygen abundance determinations. The flux in the [O III]$\lambda\lambda$4959,5007 lines is estimated as [O III]$\lambda\lambda$4959,5007 = 1.3[O III]λ5007 and the flux in the [N II]$\lambda\lambda$6548,6584 lines is estimated as [N II] λ, λ6548,6584 = 1.3[N II]λ6584 (Storey & Zeippen 2000). The R-calibration produces abundances compatible to the T_e-based abundance scale and is valid over the whole metallicity scale of H II regions.

We carried out an extensive search for galaxies with off-centered spots of enhanced σ by performing visual

[2] The NASA/IPAC Extragalactic Database (NED) is operated by the Jet Propulsion Laboratory, California Institute of Technology, under contract with the National Aeronautics and Space Administration. http://ned.ipac.caltech.edu/

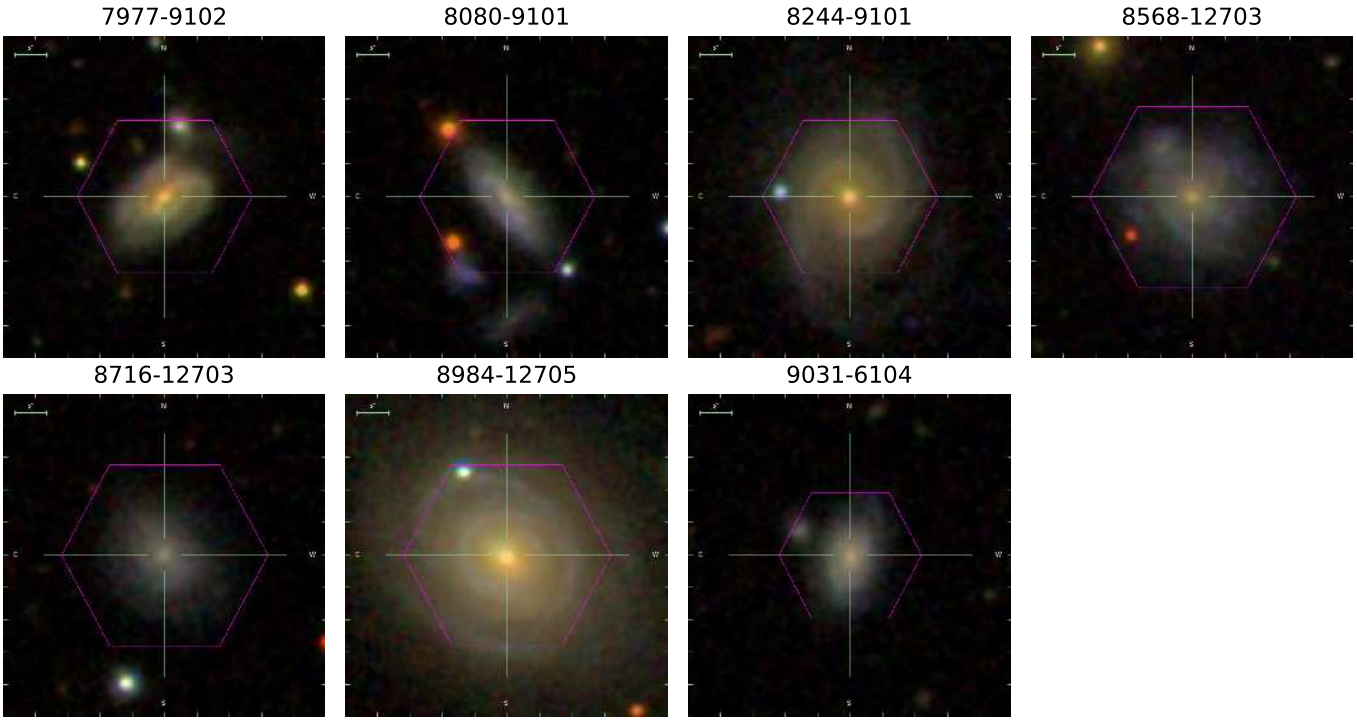

Fig. 1. Images of galaxies of our sample in the SDSS *gri* filters.

Table 1. Properties of our sample of MaNGA galaxies with the off-centered spots of the enhanced gas velocity dispersion.

MaNGA number	Other name	RA (°)	Dec (°)	i (°)	$\log M_{sp}$ ($M_\odot$)	R_{25} (Kpc)	d (Mpc)	R_{spot} (R_{25})	BPT_{center}	BPT_{spot}
7977–09102		332.830664	12.184717	41.9	10.935	12.8	251.4	1.0	1	1
8080–09101		47.340029	−0.407944	57.3	9.881	10.5	180.3	1.0	0	0
8244–09101	PGC 25036	133.787581	52.470442	27.4	11.201	18.7	241.6	0.8	0	0
8568–12703		156.810365	38.204502	26.6	10.469	14.5	221.2	0.8	0	0
8716–12703		122.411182	54.552173	43.1	9.770	9.3	174.5	0.7	0	2
8984–12705	NGC 5251	204.353484	27.419218	36.5	11.292	20.3	158.3	0.6	2	0
9031–06104		240.585568	44.470175	41.7	10.019	8.5	185.1	0.9	0	0

Notes. The columns show the MaNGA number, the other name, the right ascension (RA) and the declination (Dec) (J2000.0), the kinematic inclination angle i, the spectroscopic stellar mass M_{sp} in solar masses, the optical radius R_{25} in kpc, the galaxy distance d in Mpc, the galactocentric distance (normalized to the optical radius R_{25}) of the spot position, the BPT type of the radiation at the center of the galaxy (0 – SF, 1 – intermediate, 2 – AGN), the BPT type of the radiation in the spot of the enhanced gas velocity dispersion.

examination of the σ maps of about three thousands galaxies from the SDSS DR15 MaNGA survey but we do not pretend that our list is exhaustive. The visual selection of spots with enhanced gas velocity dispersion is somewhat arbitrary. Our preliminary list includes 14 MaNGA galaxies with off-centered spots of enhanced gas velocity dispersion σ. There is a variation in the values of σ across the image of each galaxy. The variation of σ can form a global structure: the σ distribution can show a band of enhanced σ along the minor axis in the image (Pilyugin et al. 2021), and the value of the gas velocity dispersion is usually enhanced at the center of the galaxy (Pilyugin et al. 2020a). There is a chaotic variation in the σ in addition to the global variation. The amplitude of the chaotic variation of the σ is more or less similar over the whole image of the galaxy. In some MaNGA galaxies, however, we identify off-centered spots of enhanced gas velocity dispersion where the σ enhancement in the spot is significantly higher than the amplitude of the chaotic variation.

Seven galaxies of the preliminary list were excluded from futher consideration for the following reasons. In three galaxies we find that the emission lines in the spectra of the spaxels within the spots are double or double-peaked (M-8553-09102, M-9029-12705, and M-9049-12701). Those galaxies were excluded from our current sample since the large widths of the emission line profiles correspond to two Gaussians, and not one. We find that the validity of some line measurements in the spots of four galaxies is not beyond the question. Those galaxies were also excluded from the current consideration.

3. Results

3.1. The properties of galaxies obtained using our measurements

Our final list includes seven galaxies. Figure 1 shows the images of the galaxies. Table 1 lists the general characteristics of each

galaxy. The first column gives its MaNGA number. The second column gives other known names. We have indicated the most widely used name for each galaxy, with the following categories in descending order:
NGC – New General Catalogue,
UGC – Uppsala General Catalog of Galaxies,
PGC – Catalogue of Principal Galaxies.
The right ascension (RA) and declination (Dec) (J2000.0) of each galaxy are given in Cols. 3 and 4. The right ascension and declination are taken from the NASA/IPAC Extragalactic Database (NED). The kinematic inclination angles determined in this paper are listed in Col. 5. The spectroscopic stellar masses M_{sp}, in solar masses, are reported in Col. 6. The optical radius R_{25} in Kpc determined here are given in Col. 7. The adopted distances (taken from the NED) are reported in Col. 8. The galactocentric distances (normalized to the optical radius R_{25}) of the spot position are listed in Col. 9. The BPT type of radiation at the center of the galaxy (0 – SF, 1 – intermediate, 2 – AGN) and the BPT type of radiation in the spot are given in Cols. 10 and 11, respectively.

The maps of the surface brightness, the line-of-sight velocity, the oxygen abundance, the gas velocity dispersion, and the BPT types of the spectra for the MaNGA galaxies in our sample are shown in Figs. A.1–A.7. The location of the spot is labeled with a circle. It should be noted that the circle is not the boundary of the spot but shows the point spread function (PSF) of the MaNGA measurements which is estimated to have a full width at half maximum of 2.5 arcsec, or 5 pixels (Bundy et al. 2015; Belfiore et al. 2017). The location of the center of the spot is estimated by eye and is somewhat arbitrary. The comments to individual galaxies are given below.

M-7977-09102. This is a giant galaxy of mass $10^{10.935}\,M_\odot$ at a distance of 251.4 Mpc. The M-7977-09102 galaxy has a close satellite (SDSS J221119.18+121116.0) of mass $10^{9.489}\,M_\odot$. The separation between M-7977-09102 and its satellite galaxy on the sky plane is ∼14 Kpc (that is comparable to the optical radius of M-7977-09102, R_{25} = 12.8 Kpc) and the separation in the line-of-sight velocity is $dV_{los} \sim 230\,km\,s^{-1}$ (that is comparable with the variation of the V_{los} across the image of M-7977-09102, see panel b of Fig. A.1). The field of view of the MaNGA measurement covers partly the satellite. The enhanced gas velocity dispersion takes place in the region at the edge of M-7977-09102, which is close to the satellite. The emission lines in the spectra of the spaxels within the spot of the enhanced gas velocity dispersion are single-peaked, see panels f2 and f3 of Fig. A.1. This evidences against a false enhancement of the lines width due to two separate lines (M-7977-09102 and satellite). Some spaxels in the spot show the spectra of intermediate BPT type.

M-8080-09101. This galaxy has a mass of $10^{9.891}\,M_\odot$, and it is at a distance of 180.3 Mpc. The M-8080-09101 galaxy has a close satellite (SDSS J030922.02-002440.5) of mass $10^{9.489}\,M_\odot$. The separation between the M-8080-09101 galaxy and its satellite in the sky plane is comparable to the optical radius of M-8080-09101, and the separation in the line-of-sight velocity is comparable to the variation of the V_{los} across the image of M-8080-09101, see panel b of Fig. A.2. The field of view of the MaNGA measurement covers partly the satellite. The enhanced gas velocity dispersion can be seen in both, the region of M-8080-09101 which is close to the satellite, and the region of the satellite which is close to M-8080-09101. The lines in the spectra of the spaxels with enhanced gas velocity dispersion are single-peaked, see panels f2 and f3 of Fig. A.2. The gas-phase oxygen abundance in the satellite is lower by a factor of around three as compared to the oxygen abundance in M-8080-09101 (panel c of Fig. A.2). However, the oxygen abundance at the edge of the satellite close to M-8080-09101 is higher than in the rest of the satellite. This can be an indicator of the gas exchange between M-8080-09101 and its satellite. Unfortunately, the spectra of the spaxels in the region between M-8080-09101 and the satellite are noisy, which prevents the determination of the oxygen abundances and the further investigation of a detailed picture of gas exchange between those galaxies.

M-8244-09101. This galaxy has a mass of $10^{11.201}\,M_\odot$, and it is at a distance of 241.6.7 Mpc. There is a spot of enhanced gas velocity dispersion at a galactocentric distance of around 15 Kpc (∼0.8 of the optical radius R_{25}, panels d1 and d2 of Fig. A.3). The gas-phase oxygen abundance in the spot is lower in comparison to the abundance at this radius (panels d1 and d2 of Fig. A.3). The lines in the spectra of the spaxels with enhanced gas velocity dispersion are single-peaked, see panels f2 and f3 of Fig. A.3.

M-8568-12703. This galaxy has a mass of $10^{10.469}\,M_\odot$ and it is at a distance of 221.2 Mpc. There is a large spot of enhanced gas velocity dispersion at a galactocentric distance of around 11 Kpc (∼0.8 of the optical radius R_{25}, panels d1 and d2 of Fig. A.4). The spot is also revealed on the surface brightness and the line-of-sight velocity maps. The lines in the spectra of the spaxels with enhanced gas velocity dispersion are single-peaked, see panels f2 and f3 of Fig. A.4.

M-8716-12703. This galaxy has a mass of $10^{9.770}\,M_\odot$ and it is at a distance of 174.5 Mpc. There is a spot of enhanced gas velocity dispersion at a galactocentric distance of around 6 Kpc (∼0.7 of the optical radius R_{25}, panels d1 and d2 of Fig. A.5). The configuration of the radiation distribution in the spot resembles the configuration of the radiation distribution in a circumnuclear AGN, that is the innermost region of the AGN-like radiation is surrounded by a ring of radiation of the intermediate type (panel e of Fig. A.5). The spot is not exhibited appreciable on the surface brightness and the line-of-sight velocity maps. The lines in the spectra of the spaxels with enhanced gas velocity dispersion are single-peaked, see panels f2 and f3 of Fig. A.5.

M-8984-12705. Also known as NGC 5251, this galaxy is an isolated S0-a (HyperLeda database) galaxy of mass $10^{11.292}\,M_\odot$ at a distance of 158.3 Mpc. There is a spot of enhanced gas velocity dispersion at a galactocentric distance of around 12 Kpc (∼0.6 of the optical radius R_{25}, panels d1 and d2 of Fig. A.6). The gas-phase oxygen abundance in the spot is reduced in comparison to the abundance at this radius (panel c of Fig. A.6). The spot is also a prominent feature on the surface brightness map. The complexity of the Hα line profile provides evidence that the radiation is originated in several clumps, that is several gas fragments from the satellite are mixed to the interstellar medium of the disk and each fragment produces different enhancements of gas velocity dispersion and/or different changes in the line-of-sight velocity. However, the disagreement between Hα and Hβ line profiles (see panels f2 and f3 of Fig. A.6) prevents a solid interpretation of the origin of the interaction. The spaxel spectra in the spot are noisy, more accurate (with higher spectral resolution) measurements are necessary to make a solid conclusion.

M-9031-06104. This galaxy has a mass $10^{10.019}\,M_\odot$ and it is at a distance of 185.1 Mpc. The M-9031-06104 galaxy has a close satellite. The separation between M-9031-06104 and its satellite exceeds slightly the optical radius of M-9031-06104 (R_{25} = 8.5 Kpc), the line-of-sight velocities of M-9031-06104 and its satellite are close to each other, Fig. A.7. The field of

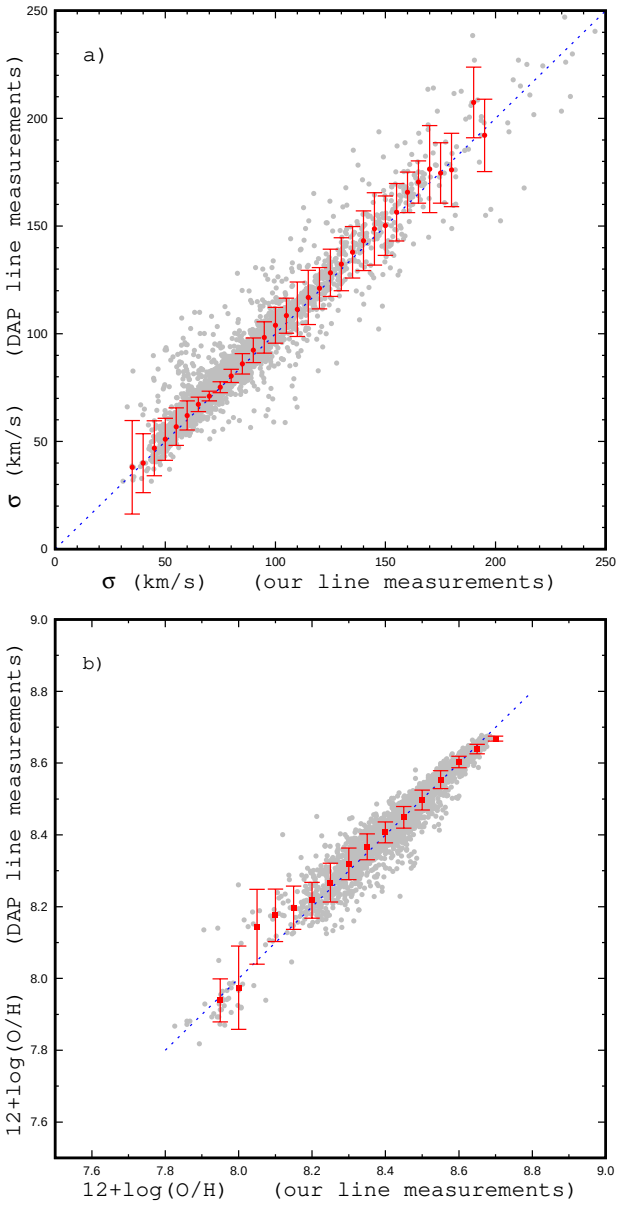

Fig. 2. Comparison between the MANGA-DAP and our measurements for the values of the gas velocity dispersion σ and the oxygen abundance O/H. *Panel a*: the grey points show the gas velocity dispersion of individual spaxels. The red points show the mean values of velocity dispersion in bins of 5 km s^{-1}. *Panel b*: the grey points show the oxygen abundance of individual spaxels. The red points show the mean values of oxygen abundance in bins of 0.05 dex. In both panels the dotted-line is the one-to-one relation.

view of the MaNGA measurement covers partly the satellite. The enhanced gas velocity dispersion takes place at the edge of M-9031-06104 which looks to the satellite. The emission lines in the spectra of the spaxels with enhanced gas velocity dispersion are single-peaked, see panels f2 and f3 of Fig. A.7.

3.2. The properties of galaxies obtained using the MaNGA Data Analysis Pipeline (DAP) measurements

The emission line parameters for our sample of galaxies are available from the MaNGA data analysis pipeline (DAP) measurements. We use the datacubes from the most recent publicly available data release DR16, which is based on the DAP version v2.4.3. The important difference between the DAP measurements and ours is that DAP is fitting all emission lines simultaneously with tied line centers and line widths. For each spaxel spectrum, we take the fluxes of the [O II]$\lambda\lambda$3727,3729, Hβ, [O III]λ5007, Hα, and [N II]λ6584 emission lines, the line-of-sight velocity and the gas velocity dispersion derived from the Hα line from the datacube with HYB10 binning scheme. In this case a Voronoi binning of $S/N = 10$ is applied to the stellar spectra which is then used for the stellar kinematics. The bins are then deconstructed such that the emission-lines fitting is measured on the individual spaxels.

We also take the photometric inclination angle and the position angle of the major photometric axis for each galaxy from the NASA-Sloan Atlas (NSA) catalog[3]. Both angles are obtained from the Sersic fit to the surface brightness profile in the r band.

The maps of the line-of-sight velocity, the oxygen abundance, the gas velocity dispersion, and the BPT types of the spectra for our sample of MaNGA galaxies were constructed using the DAP measurements. The maps are shown in Figs. B.1–B.7. A visual comparison between the maps based on our measurements (Figs. A.1–A.7) and the maps based on the DAP measurements (Figs. B.1–B.7) shows that there is a satisfactory agreement. It should be emphasized however that the DAP measurements within the spots of two galaxies (M-8244-09101 and M-8984-12705) are not available.

Here we show a quantitative comparison between spaxel properties based on ours and DAP measurements. Panel a of Fig. 2 shows the comparison between the gas velocity dispersion σ from DAP vs. our measurements. The grey points correspond to 13 219 individual spaxels in seven galaxies, while the red points are the mean values of velocity dispersion in bins of 5 km s^{-1}. The bars denote the mean value of the scatter of the σ in each bin. Only bins containing five or more points are shown. The mean value of the scatter of the gas velocity dispersion around the one-to-one relation is ~5 km s^{-1}. This value can be used to specify the uncertainty in the values of the gas velocity dispersion. Inspection of panel a of Fig. 2 shows that our values of the gas velocity dispersion and the values from the DAP measurements are in satisfactory agreement. There is no appreciable systematic difference between $\sigma_{\rm our}$ and $\sigma_{\rm DAP}$ values over the whole interval of σ, that is, the $\sigma_{\rm our}$–$\sigma_{\rm DAP}$ diagram follows well the one-to-one relation.

Panel b of Fig. 2 shows the comparison between the determined oxygen abundances from the DAP and our measurements. The grey points are the data of 6979 individual spaxels in seven galaxies. The red points indicate the mean values of oxygen abundances in bins of 0.05 dex. The mean value of the scatter of the oxygen abundance around equal-value line is ~0.025 dex. This value can serve as an estimation of the uncertainty in the values of the oxygen abundance. Inspection of panel b of Fig. 2 shows that values of the oxygen abundances determined from our and the DAP measurements are in satisfactory agreement over the whole interval of metallicities.

Panel a1 of Fig. 3 shows the difference between the values of the gas velocity dispersion from the DAP and our measurements d$\sigma = \sigma_{\rm DAP}$–$\sigma_{\rm our}$ as a function of H$_\alpha$ flux for all the spaxels. The measured (non-deredddened) Hα fluxes in units of 10^{-17} erg s^{-1} cm^{-2} spaxel^{-1} is presented. The grey points show the dσ for the individual spaxels, while the red points are the mean values of dσ in bins of 0.2 dex in H$_\alpha$ flux. The bars denote the mean value of the scatter of the dσ in each bin. Inspection of panel a1 of Fig. 3 shows that the mean values of dσ are close to

[3] http://nsatlas.org

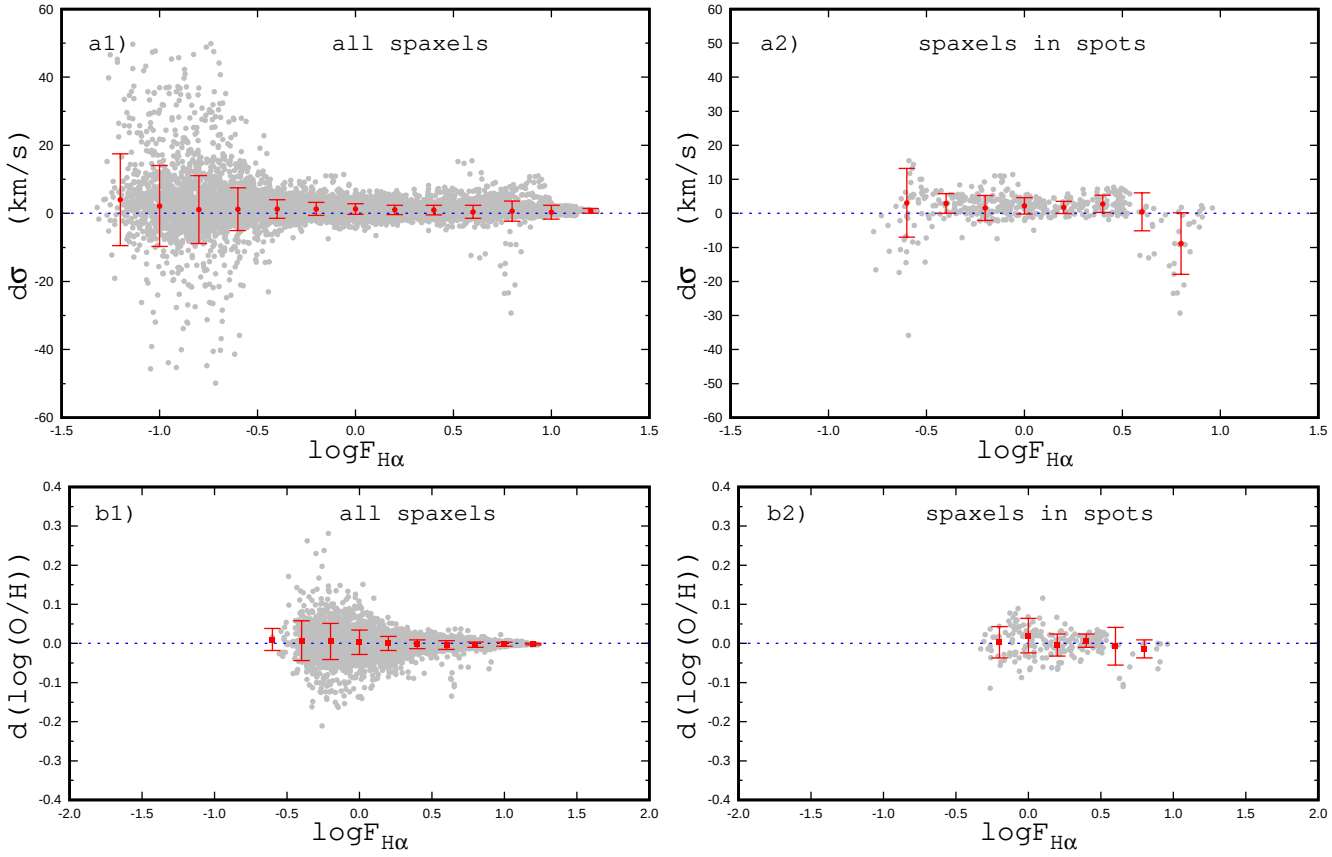

Fig. 3. Difference between the DAP and our measurements of the gas velocity dispersion σ and the oxygen abundance O/H. *Panel a1*: the grey points show the difference $d\sigma = \sigma_{DAP} - \sigma_{our}$ as a function of H_α flux for all the individual spaxels in seven galaxies. The red points show the mean values of the difference in bins of 0.2 dex in H_α flux. *Panel a2*: same as panel a1 but for the spaxels in the spots. *Panel b1*: the grey points show the difference $d(O/H) = \log(O/H)_{DAP} - \log(O/H)_{our}$ as a function of H_α flux for all the individual spaxels. The red points show the mean values of difference in bins of 0.2 dex in H_α flux. *Panel b2*: same as panel b1 but for the spaxels in the spots.

zero over the whole range of Hα fluxes, while the scatter in dσ is larger for low Hα fluxes.

It is interesting to examine the values of the dσ for the spaxels in the spots of enhanced gas velocity dispersion. It is impossible to determine the exact location of the center of the spot and its border since the measurements are usually available for only the part of the spot (see, for example, Fig. A.2). Then we consider the regions outlined by rings in Figs. A.1–A.7 as the spots and examine the values of the dσ for the spaxels within those regions. Panel a2 of Fig. 3 shows the dσ as a function of H_α flux for the spaxels in the spots. The grey points denote the dσ for the individual spaxels, while the red points are the binned mean values of dσ. The bars denote the scatter of the dσ in each bin. Inspection of panel a2 of Fig. 3 shows that the values of the dσ in the spaxels within the spots are similar to that in the spaxels outside the spots. The values of the dσ for the majority of the spaxels in the spots are less than $\sim$6 km s^{-1} for the galaxies considered.

Panel b1 of Fig. 3 shows the difference between the values of the oxygen abundance determined from the DAP and our measurements $d(O/H) = \log(O/H)_{DAP} - \log(O/H)_{our}$ as a function of the H_α flux for all the spaxels. The grey points show the d(O/H) for the individual spaxels, while the red points are the mean values of d(O/H) in bins of 0.2 dex in H_α flux. Inspection of panel b1 of Fig. 3 shows again that mean values of the d(O/H) are close to zero over the whole range of Hα fluxes, while the scatter in d(O/H) is larger at low Hα fluxes. Panel b2 of Fig. 3 shows the d(O/H) as a function of H_α flux for the spaxels in the spots. Inspection of this panel shows that the values of the d(O/H) of the spaxels within the spots are similar to those of the spaxels outside the spots. The values of the d(O/H) for the majority of the spaxels in the spots are less than $\sim$0.05 dex for the galaxies considered.

The geometrical parameters of galaxies (coordinates of the rotating center Xo and Yo, the position angle of the major kinematic angle PA_{kin}, and the inclination angle i_{kin}) were derived using both, our and DAP line-of-sight velocity fields. In addition, the photometric inclination angle i_{phot} and the position angle of the major photometric axis PA_{phot} for each galaxy were taken from the DAP data. Then we can compare the two sets of coordinates for the rotating center (e.g., $dXo = Xo_{DAP} - Xo_{our}$) and three sets of inclination and position angles (e.g., $dPA_{kin-kin} = PA_{kin,DAP} - PA_{kin,our}$ and $dPA_{phot-kin} = PA_{phot} - PA_{kin,our}$). Panel a of Fig. 4 shows the dXo and dYo as a function of the kinematic inclination angle. Inspection if this panel shows that the values of dXo and dYo are usually within $\sim$0.2 and $\sim$0.4 spaxel for the galaxies considered here. Panel b of Fig. 4 shows the values of the $di_{kin-kin}$ and $di_{phot-kin}$ as a function of the kinematic inclination angle. Inspection of this panel shows that the values of $di_{kin-kin}$ are within $\sim$4° while the values of $di_{phot-kin}$ can reach up to $\sim$12°. Panel c of Fig. 4 shows the values of the $dPA_{kin-kin}$ and $dPA_{phot-kin}$ as a function of the kinematic inclination angle. Inspection of this panel shows that the values of $dPA_{kin-kin}$ are within $\sim$1° while the values of $dPA_{phot-kin}$

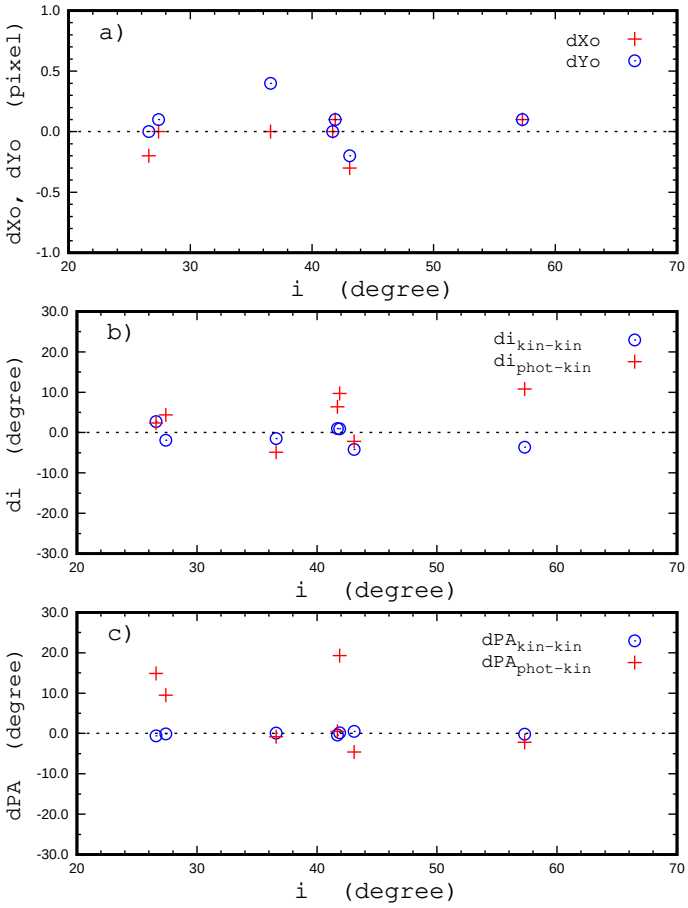

Fig. 4. Comparison between the different sets of geometrical parameters for our sample of galaxies. *Panel a*: differences between the coordinates of the kinematical center of galaxies dXo and dYo derived using DAP and our measurements. *Panel b*: differences between two determinations of the kinematical inclination angle, and between the kinematic and photometric inclination angles. *Panel c*: differences between two determinations of the position angle of the major kinematical axis, and between the position angles of the major axis and the major photometric axis. See text for details.

can reach up to ∼20°. The geometrical parameters of galaxies derived from the analysis of the line-of-sight velocity field are rather robust. This can be attributed to the fact that an iterative procedure is used in the determination of the geometrical parameters and rotation curve, that is, the points with large deviations from the rotation curve are rejected.

Thus, the properties of the gas in the spaxels derived using our and the DAP measurements are in satisfactory agreement. There is no systematic difference between the σ_{our} and σ_{DAP} values over the whole interval of σ, that is the σ_{our}–σ_{DAP} diagram follows well the one-to-one relation. There is not a significant difference between $(O/H)_{our}$ and $(O/H)_{DAP}$ values over the whole interval of metallicity, that is the $(O/H)_{our}$–$(O/H)_{DAP}$ diagram also follows the one-to-one relation. Hence, the quantities based on our measurements are used below.

4. Discussion

The following questions are discussed in this Section. First we discuss the evidences in favor of that the spots of enhanced gas velocity dispersion in six galaxies of our sample can be caused by (minor) mergers or interactions. Then we examine whether the presence of the spot of enhanced σ is accompanied by the enhancement of the median value of the gas velocity dispersion in the host galaxy, that is whether the minor interaction (or merger) results in the disturbance of the gas velocity dispersion in a localize region or in the galaxy as whole. Finally, we discuss the spot of enhanced σ in the galaxy M-8716-12703 with AGN-like configuration of the radiation distribution. This spot is compared with the AGN in the galaxy M-8984-12705.

4.1. Minor merger or interaction as a reason for the spot of enhanced σ

Three galaxies in our sample (M-7977-09102, M-8080-09101, and M-9031-06104) have a very close satellite (see the images for those galaxies in Fig. 1, and the maps of the surface brightness and line-of-sight velocity distributions across the images in Figs. A.1, A.2, and A.7, as well as the comments for those galaxies above). The separation in the sky plane is comparable to the optical radius of the galaxy in each case, and the separation in the line-of-sight velocity is comparable to the variation of the V_{los} across the image of the galaxy. The spots of the enhanced σ in those galaxies are located at the edge of the galaxy close to the satellite. This suggests that the spots of the enhanced σ in those galaxies are caused by the interaction with the satellite (gas flow from the satellite).

The spots of enhanced σ in four other galaxies (M-8244-09101, M-8568-12703, M-8716-12703, and M-8984-12705) are located within the optical radius, at the fractional radii from ∼0.6 to ∼0.8 optical radius. The spots of the enhanced σ in three of those galaxies are related to the bright spots in the photometric B band (see images for those galaxies in Fig. 1, and the maps of the surface brightness across the images for those galaxies in Figs. A.3, A.4, and A.6, as well as the comments for those galaxies above). This could be an indicator of a projection of a satellite on the galaxy. It was noted above that the projection of a satellite on the galaxy takes indeed place in three galaxies (M-8553-09102, M-9029-12705, and M-9049-12701) from our preliminary list. Two sets of the emission lines are present in the spectra of the spaxels within the spots in two galaxies M-8553-09102 and M-9029-12705, that is, both set of emission lines of the galaxy and its satellite are detected. The emission lines in the spectra of the spaxels within a spot in the galaxy M-9049-12701 are double-peaked, see panels f2 and f3 of Fig. A.8. Those galaxies were excluded from the current consideration. Regarding the three galaxies in our final list with enhanced σ spots associated to the bright B band spots we find the following. A minor (if any) separation in the line-of-sight velocity between the spot and the surroundings, as well as the single-peaked emission lines in the spaxel spectra in the spot suggest that the emission lines in the spectra of the spaxels in the enhanced σ spot originate in a single region located within (or at least very close to) the disk. Thus either the satellite is already captured and is in the disk of the galaxy, or the region of enhanced σ is caused by the interaction with a satellite (gas infall from the satellite onto the disk of the galaxy). The oxygen abundances in the spots of enhanced σ in these three galaxies are reduced, this is a strong evidence in favor of that the low-metallicity gas from the satellite is mixed with the gas of the galactic disk.

The spectra of the spaxels within a spot are usually H II-region-like. This suggests that the gas infall onto the galaxy does not necessarily result in appreciable shocks. In contrast, the spot of enhanced σ in the galaxy M-8716-12703 is associated with an off-centered AGN-like configuration of the radiation

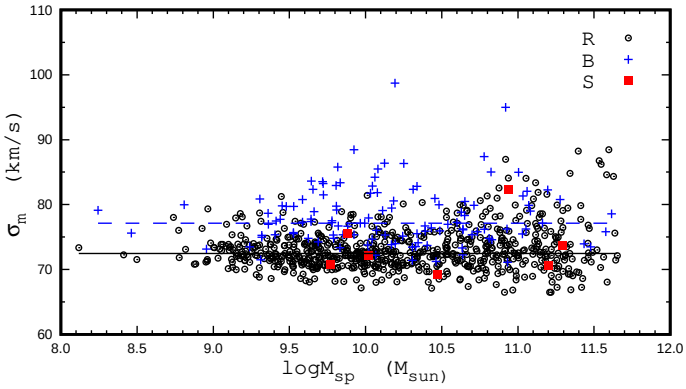

Fig. 5. Median values of gas velocity dispersion σ_m in galaxies. The black circles show σ_m as a function of the spectroscopic stellar mass M_{sp} for individual galaxies with the R distribution, the blue plus signs denote galaxies with the B distribution, and red squares galaxies with the spots of enhanced σ. The solid line shows the median value of σ_m in galaxies with the R distribution, and the dashed line shows the median value of σ_m for galaxies with the B distribution. The σ_m for galaxies with R and B distributions are from Pilyugin et al. (2021).

distribution, in the sense that the innermost region of the AGN-like radiation is surrounded by a ring of radiation of the intermediate type. There are no evident signs of gas infall onto this galaxy. One can suggest that the spot of enhanced σ in the galaxy M-8716-12703 is different in origin or that the type the interaction (gas infall onto the galaxy) in this case differs from that in other galaxies.

It is known that the gas velocity dispersion in the giant H II region correlates with the Hα luminosity or diameter, in the sense that the σ is higher in the H II region with a higher Hα luminosity or larger diameter (Terlevich & Melnick 1981; Fernández et al. 2018). There is the minimum value of the gas velocity dispersion in H II regions of a given Hα luminosity or diameter for H II regions with a Hα luminosity higher than $\sim 10^{38}$ erg s^{-1} (Relaño et al. 2005; Zaragoza-Cardiel et al. 2015; Ambrocio-Cruz et al. 2016). The integral emission line profile of a giant H II region measued at low resolution is rather smooth and well fitted by a Gaussian, while the observations at high spatial and spectral resolution reveal that a giant H II region breaks up into many discrete components (Chu & Kennicutt 1994; Bresolin et al. 2020). The H II regions from interacting galaxies show, on average, higher gas velocity dispersions than those from isolated galaxies (Zaragoza-Cardiel et al. 2015). The diameters of the largest giant H II regions in galaxies are ~1 kpc (Kennicutt 1988; Zaragoza-Cardiel et al. 2015). The minimum observed size of the spots of enhanced σ considered is ~6 pixels (only part of the spots is usually measured). The distances of galaxies of our sample are from 158 to 251 Mpc (see Table 1), which give a scale of ~0.4–0.6 kpc pixel^{-1}, meaning that the observed sizes of the spots are larger than ~2.5 kpc. Thus, the sizes of the spots of enhanced σ we considered exceed the sizes of the largest known H II regions. However, the observed sizes of the spots are comparable to the point spread function (PSF) of the MaNGA measurements which is estimated to have a full width at half maximum of 5 pixels (Bundy et al. 2015; Belfiore et al. 2017). Therefore, the measurements of the spots with a higher resolution and higher S/N are necessary to make accurate estimations of their sizes (and other characteristics) and to perform the quantitative comparison between spots and giant H II regions.

4.2. Relation between presence of spot and enhancement of σ in whole galaxy?

Above we have discussed evidences in favor that the off-centered spots of enhanced σ in galaxies can be caused by (minor) mergers or interactions. Here we consider the median values of the gas velocity dispersion σ_m in galaxies as a whole aiming to examine whether there is a difference between galaxies with and without spots of enhanced σ. The red squares in Fig. 5 show the median values of the observed gas velocity dispersion σ_m as a function of the spectroscopic stellar mass M_{sp} for our sample of galaxies with the spots of enhanced σ. A sample of galaxies from Pilyugin et al. (2021) is used for comparison. Since the median value of the gas velocity dispersion σ_m in a galaxy is related to the type of distribution of the gas velocity dispersion σ across its image (in the sense that the σ_m in galaxies with B distribution is higher by around 5 km s^{-1}, on average, than that of galaxies with R distribution), then we distinguish the galaxies with R and B distributions in the comparison sample. Figure 5 shows the median value of the observed gas velocity dispersion σ_m as a function of the spectroscopic stellar mass M_{sp} for galaxies with the R distribution (black circles) and for galaxies with the B distribution (blue plus signs). The solid line in Fig. 5 denotes the median value of the σ_m for the R distribution (72.45 ± 3.24 km s^{-1}), while the dashed line corresponds to the B distribution (77.15 ± 4.66 km s^{-1}).

Examination of Fig. 5 shows that the σ_m in six out of seven galaxies with the spots of enhanced σ is close to the typical value of the σ_m in galaxies without the spots of enhanced σ. On the other hand, the value of one galaxy with the spot of enhanced σ (M-7977-09102) is slightly higher than the typical value of the σ_m in galaxies without the spots of enhanced σ. This can be considered as an evidence in favor of that the minor interaction (or merger) results usually in the disturbance of the gas velocity dispersion in a localize region, but not in the galaxy as whole.

4.3. Spot in the galaxy M-8716-12703: comparison to AGN in galaxy M-8984-12705

The galaxy M-8984-12705 with off-centered spot of enhanced σ from our sample shows central AGN and an extended extranuclear LINERs (Low Ionization Nuclear Emission line Regions). The different sources of the ionizing photons in the LINERs are discussed. It was suggested (e.g., Stasińska et al. 2006, 2008; Sarzi et al. 2010; Yan & Blanton 2012; Singh et al. 2013) that the radiation of the hot, low-mass evolved (post-asymptotic giant branch) stars (HOLMES) can be the source of the ionizing photons in the LINERs. It was argued (Heckman 1980; Dopita & Sutherland 1995; Ho et al. 2014; Molina et al. 2018) that a LINER can be also excited by the shocks caused by different phenomena (jets, galactic winds, galaxy-galaxy interactions). Monreal-Ibero et al. (2006, 2010) have studied an extended extranuclear LINERs in ultraluminous infrared galaxies. They revealed a positive correlation between the gas velocity dispersion and the diagnostic emission line ratios of the BPT diagram. This correlation is interpreted as a signature of shock excitation, where shocks are driven by galaxy mergers or interactions (Monreal-Ibero et al. 2006, 2010; Rich et al. 2014, 2015).

Panel a in Fig. 6 shows the distribution of the flux in the Hα line across the image of the galaxy M-8984-12705 (NGC 5251). We use the de-reddened flux in the Hα line per spaxel $F_{H\alpha}$ in units 10^{-17} erg s^{-1} cm^{-2} spaxel^{-1} (not corrected for the galaxy inclination) since only the relative variation of the surface brightness in the Hα line within the galaxy is considered. Further,

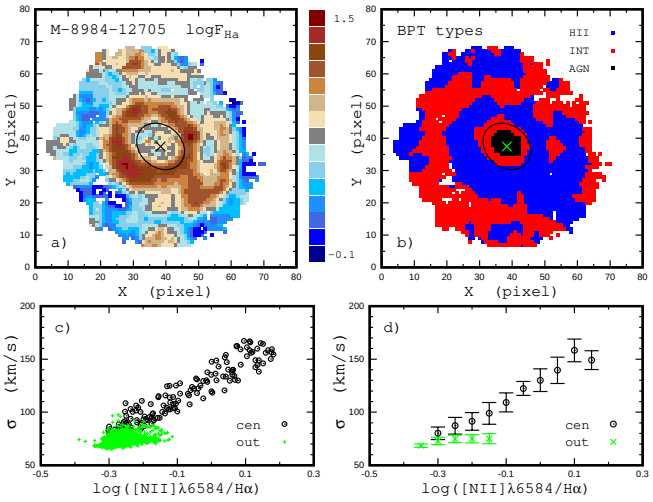

Fig. 6. Properties of the galaxy M-8984-12705 with central AGN and extranuclear LINERs. *Panel a*: distribution of the Hα flux (in logarithmic scale) in the spaxel spectra across the image of the galaxy. The value of the flux is color-coded. The cross shows the kinematic center of the galaxy, the ellipse outlines the adopted circumnuclear region. *Panel b*: locations of the spaxels with spectra of different BPT types (the AGN-like, H II-region-like, and intermediate) on the image of the galaxy. *Panel c*: relation between gas velocity dispersion σ and [N II]λ6584/Hα line ratio for individual spaxels with intermediate and AGN-like spectra in the circumnuclear (dark circles) and in the extranuclear (green plus signs) regions of the galaxy M-8984-12705. *Panel d*: median values of σ for spaxels in bins of 0.05 dex in [N II]λ6584/Hα for spaxels in the circumnuclear (dark circles) and in the extranuclear (green crosses) regions.

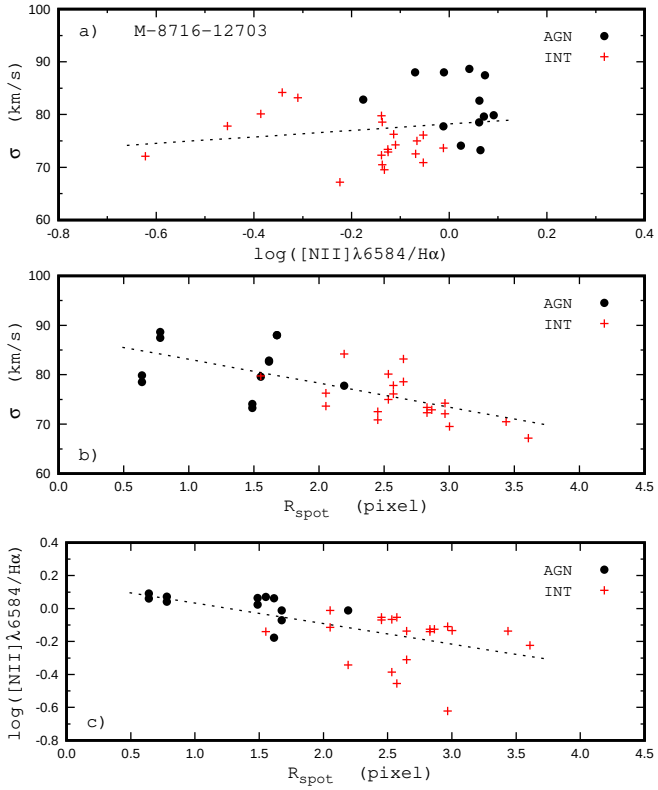

Fig. 7. Properties of the off-centered AGN-like spot in the galaxy M-8716-12703. *Panel a*: relation between gas velocity dispersion σ and [N II]λ6584/Hα line ratio for individual spaxels with the AGN-like (circles) and the intermediate (plus signs) spectra in the spot. *Panel b*: gas velocity dispersion as a function of the distance to the center of the spot R_{spot} for those spaxels. *Panel c*: [N II]λ6584/Hα line ratio as a function of the distance to the center of the spot.

since the current star formation rate is commonly estimated from the Hα luminosity of a galaxy using the calibration relation of Kennicutt (1998) then the panel a in Fig. 6 can be interpreted as a map of the relative variation of the current star formation rate (in arbitrary units) within the galaxy. A prominent feature in the distribution of the Hα flux in the image of the galaxy M-8984-12705 is the presence of a bright ring.

Panel b in Fig. 6 shows the locations of the spaxels with spectra of different BPT types (the AGN-like, H II-region-like, and intermediate) on the image of the galaxy M-8984-12705. A comparison between panel a and panel b in Fig. 6 shows that the spaxel spectra are H II-region-like in the areas of high star formation rate, and that the spectra are intermediate or AGN-like types correspond to areas of low Hα flux. The galaxy M-8984-12705 hosts the AGN at its center and extranuclear LINERs-type regions.

Next, we examine the relationships between the gas velocity dispersion σ and [N II]λ6584/Hα line ratio for the central AGN and the extranuclear LINERs in the M-8984-12705 galaxy. Panel d of Fig. A.6 shows that the observed gas velocity dispersion σ decreases with galactocentric distance up to some radius within this galaxy and remains approximately constant beyond this radius. The radius where the break occurs is adopted as the radius of the central AGN. The ellipses in panels a and b of Fig. 6 outline the central AGN in the image of the galaxy M-8984-12705.

Panel c in Fig. 6 shows the relation between gas velocity dispersion σ and [N II]λ6584/Hα line ratio for individual spaxels in the central AGN (dark circles) and in the extranuclear (green plus signs) LINERs of M-8984-12705. Panel d shows the median values of σ for those spaxels in bins of 0.05 dex in [N II]λ6584/Hα for spaxels in the central AGN (dark circles) and in the extranuclear (green crosses) LINERs. Examination of Fig. 6 shows a correlation between the gas velocity dispersion σ and the [N II]λ6584/Hα line ratio that takes place only for the central AGN in the M-8984-12705 galaxy. According to Monreal-Ibero et al. (2006, 2010) and Rich et al. (2014, 2015), the lack of an appreciable correlation between gas velocity dispersion σ and [N II]λ6584/Hα line ratio for extranuclear LINERs can be considered as evidence that shocks do not play an appreciable role in their excitation. This is in line with our above conclusion that a (minor) merger or interaction does not necessary result in appreciable shocks.

Here we examine properties of the off-centered AGN-like spot in M-8716-12703. The correlation between the gas velocity dispersion σ and the [N II]λ6584/Hα line ratio for individual spaxels in the spot for M-8716-12703 is only marginal (if any), the correlation coefficient is equal to 0.176, panel a in Fig. 7. At the same time, both the gas velocity dispersion σ and the [N II]λ6584/Hα line ratio show a systematic change with the distance to the center of the spot. The correlation coefficient of the relation between the gas velocity dispersion σ and the distance to the center of the spot is equal to -0.66, panel b in Fig. 7. The correlation coefficient of the relation between the [N II]λ6584/Hα line ratio and the distance to the center of the spot is equal to -0.60, panel c in Fig. 7. Thus, the properties of the off-centered AGN-like spot in the galaxy M-8716-12703 are controversial. From one hand, the radiation distribution configuration of the off-centered spot in the galaxy M-8716-12703 is

similar to that of the central AGN in the galaxy M-8984-12705, in both cases the innermost region of the AGN-like radiation is surrounded by a ring of radiation of the intermediate type. On other hand, the relation between the gas velocity dispersion σ and the [N II]λ6584/Hα line ratio for individual spaxels in the spot in M-8716-12703, is similar to that of the extranuclear LINER in the galaxy M-8984-12705, and differs strongly from that for the central AGN in the galaxy M-8984-12705.

The supernova remnants (SNRs) spectra (e.g., Long et al. 2019) are of the AGN-like or the intermediate BPT types. The SNRs exibit the gas velocity dispersion higher than that in H II regions (e.g., Points et al. 2019). Those characteristics of SNRs resemble that of the off-centered AGN-like spot in the galaxy M-8716-12703. However, the typical diameter of SNR population is 20–40 pc, the SNRs of diameters greater than 100 pc are rare among known SNRs (Franchetti et al. 2012; Bozzetto et al. 2017; Long et al. 2020), while the observed diameter of the off-centered AGN-like spot in M-8716-12703 is ~2.5 kpc (with a scale of ~0.42 kpc pixel^{-1} at the distance 174.5 kpc). Thus the size of the off-centered AGN-like spot in M-8716-12703 is much larger than that of the SNR.

5. Conclusions

We find off-centered spots of enhanced gas velocity dispersion σ in a subsample of MaNGA galaxies. We produce and analyze the distributions of the surface brightness, the line-of-sight gas velocity, the oxygen abundance, the gas velocity dispersion, and the Baldwin-Phillips-Terlevich (BPT) types of the spaxel spectra in seven MaNGA galaxies aiming to examine the origin of the off-centered spots of enhanced σ.

We found that the origin of the spots of enhanced gas velocity dispersion in six galaxies can be attributed to an interaction (or merger) with a close satellite. Three galaxies in our sample have a very close satellite (the separation in the sky plane is comparable to the optical radius of the galaxy). The spots of the enhanced σ in those galaxies are located at the edge of the galaxy close to the satellite. The spots of the enhanced σ in three other galaxies are related to the bright spots in the photometric B band within the galaxy. This can be an indicator of a projected satellite on the line of sight of the galaxy. The oxygen abundances in the spots in these three galaxies are reduced. This suggests that the low-metallicity gas from the satellite is mixed with the interstellar medium of the disk,

The spectra of the spaxels within a spot are usually H II-region-like. This suggests that the gas infall onto the galaxy does not necessarily result in appreciable shocks. The galaxy M-8984-12705 shows an off-centered spot of enhanced σ and extended extranuclear LINERs regions. The lack of an appreciable correlation between the gas velocity dispersion σ and the [N II]λ6584/Hα line ratio for extranuclear LINERs evidences that shocks do not play an important role in their excitation. This also suggests that (minor) mergers or interactions does not necessary result in appreciable shocks.

In contrast, the spot of enhanced σ in the galaxy M-8716-12703 is associated with an off-centered AGN-like configuration of the radiation distribution, in the sense that the innermost region of the AGN-like radiation is surrounded by a ring of radiation of the intermediate type. There is no evident sign of gas infall onto this galaxy. One can suggest that the spot of enhanced σ in the galaxy M-8716-12703 has a different origin, or that the characteristics of the interaction (gas infall onto the galaxy) in this case differs from that in other galaxies.

Acknowledgements. We are grateful to the referee for his/her constructive comments. L.S.P acknowledges support within the framework of the program of the NAS of Ukraine Support for the development of priority fields of scientific research (CPCEL 6541230)". BC, JN and MG are supported by AYA2014-58861-C3-1-P. I.A.Z acknowledges support by the National Academy of Sciences of Ukraine under the Research Laboratory Grant for young scientists No. 0120U100148. AMP is supported by AYA2017 88007 C3 2, MDM-2017-0737 (Unidad de Excelencia María de Maeztu, CAB). JMV and SDP acknowledge financial support from the Spanish Ministerio de Economía y Competitividad under grants AYA2016-79724-C4-4-P and PID2019-107408GB-C44, from Junta de Andalucía Excellence Project P18-FR-2664, and also acknowledge support from the State Agency for Research of the Spanish MCIU through the 'Center of Excellence Severo Ochoa' award for the Instituto de Astrofísica de Andalucía (SEV-2017-0709). SDP is grateful to the Fonds de Recherche du Québec – Nature et Technologies. The work is performed according to the Russian Government Program of Competitive Growth of Kazan Federal University and Russian Science Foundation, grant no. 20-12-00105. This research has made use of the NASA/IPAC Extragalactic Database, which is funded by the National Aeronautics and Space Administration and operated by the California Institute of Technology. We acknowledge the usage of the HyperLeda database (http://leda.univ-lyon1.fr). Funding for the Sloan Digital Sky Survey IV has been provided by the Alfred P. Sloan Foundation, the U.S. Department of Energy Office of Science, and the Participating Institutions. SDSS-IV acknowledges support and resources from the Center for High-Performance Computing at the University of Utah. The SDSS web site is www.sdss.org. SDSS-IV is managed by the Astrophysical Research Consortium for the Participating Institutions of the SDSS Collaboration including the Brazilian Participation Group, the Carnegie Institution for Science, Carnegie Mellon University, the Chilean Participation Group, the French Participation Group, Harvard-Smithsonian Center for Astrophysics, Instituto de Astrofísica de Canarias, The Johns Hopkins University, Kavli Institute for the Physics and Mathematics of the Universe (IPMU)/University of Tokyo, Lawrence Berkeley National Laboratory, Leibniz Institut für Astrophysik Potsdam (AIP), Max-Planck-Institut für Astronomie (MPIA Heidelberg), Max-Planck-Institut für Astrophysik (MPA Garching), Max-Planck-Institut für Extraterrestrische Physik (MPE), National Astronomical Observatories of China, New Mexico State University, New York University, University of Notre Dame, Observatário Nacional/MCTI, The Ohio State University, Pennsylvania State University, Shanghai Astronomical Observatory, United Kingdom Participation Group, Universidad Nacional Autónoma de México, University of Arizona, University of Colorado Boulder, University of Oxford, University of Portsmouth, University of Utah, University of Virginia, University of Washington, University of Wisconsin, Vanderbilt University, and Yale University.

References

Albareti, F. D., Allende, Prieto C., Almeida, A., et al. 2017, ApJS, 233, 25
Ambrocio-Cruz, P., Le Coarer, E., Rosado, M., et al. 2016, MNRAS, 457, 2048
Asari, N. V., Cid Fernandes, R., Stasińska, G., et al. 2007, MNRAS, 381, 263
Bacchini, C., Fraternali, F., Iorio, G., et al. 2020, A&A, 641, A70
Baldwin, J. A., Phillips, M. M., & Terlevich, R. 1981, PASP, 93, 5
Begeman, K. G. 1989, A&A, 223, 47
Belfiore, F., Maiolino, R., Tremonti, C., et al. 2017, MNRAS, 469, 151
Bournaud, F., Combes, F., & Jog, C. J. 2004, A&A, 418, L27
Bournaud, F., Chapon, D., Teyssier, R., et al. 2011, ApJ, 730, 4
Bozzetto, L. M., Filipović, M. D., Vukotić, B., et al. 2017, ApJS, 230, 2
Bresolin, F., Rizzi, L., Ho, I.-T., et al. 2020, MNRAS, 495, 4347
Bruzual, G., & Charlot, S. 2003, MNRAS, 344, 1000
Bundy, K., Bershady, M. A., Law, D. R., et al. 2015, ApJ, 798, 7
Cardelli, J. A., Clayton, G. C., & Mathis, J. S. 1989, ApJ, 345, 245
Chen, Y.-M., Kauffmann, G., Tremonti, C. A., et al. 2012, MNRAS, 421, 314
Chu, Y.-H., & Kennicutt, R. C. 1994, ApJ, 425, 720
Cid, Fernandes R., Mateus, A., Sodré, L., Stasińska, G., & Gomes, J. M. 2005, MNRAS, 358, 363
Dawson, K. S., Schlegel, D. J., Ahn, C. P., et al. 2013, AJ, 145, 10
de Blok, W. J. G., Walter, F., Brinks, E., et al. 2008, AJ, 136, 2648
Dib, S., Bell, E., & Burkert, A. 2006, ApJ, 638, 797
Dopita, M. A., & Sutherland, R. S. 1995, ApJ, 455, 468
Epinat, B., Amram, P., Balkowski, C., & Marcelin, M. 2010, MNRAS, 401, 2113
Fernández, Arenas D., Terlevich, E., Terlevich, R., et al. 2018, MNRAS, 474, 1250
Franchetti, N. A., Gruendl, R. A., Chu, Y.-H., et al. 2012, AJ, 143, 85
Governato, F., Willman, B., Mayer, L., et al. 2007, MNRAS, 374, 1479
Heckman, T. M. 1980, A&A, 87, 152
Ho, I.-T., Kewley, L. J., Dopita, M. A., et al. 2014, MNRAS, 444, 3894
Hopkins, P. F., Cox, T. J., Younger, J. D., & Hernquist, L. 2009a, ApJ, 691, 1168
Hopkins, P. F., Somerville, R. S., Cox, T. J., et al. 2009b, MNRAS, 397, 802

Hung, C.-L., Hayward, C. C., Yuan, T., et al. 2019, MNRAS, 482, 5125
Hunter, D. A., Elmegreen, B. G., Archer, H., Simpson, C. E., & Cigan, P. 2021, AJ, 161, 175
Johnson, H. L., Harrison, C. M., Swinbank, A. M., et al. 2018, MNRAS, 474, 5076
Kauffmann, G., Heckman, T. M., Tremonti, C., et al. 2003, MNRAS, 346, 1055
Kennicutt, R. C. 1988, ApJ, 334, 144
Kennicutt, R. C. 1998, ARA&A, 36, 189
Kewley, L. J., Dopita, M. A., Sutherland, R. S., Heisler, C. A., & Trevena, J. 2001, ApJ, 556, 121
Klessen, R. S., & Hennebelle, P. 2010, A&A, 520, A17
Kohandel, M., Pallottini, A., Ferrara, A., et al. 2020, MNRAS, 499, 1250
Krumholz, M. R., Burkhart, B., Forbes, J. C., & Crocker, R. M. 2018, MNRAS, 477, 2716
Lee, H., Skillman, E. D., & Venn, K. A. 2005, ApJ, 620, 223
Lehnert, M. D., Le Tiran, L., Nesvadba, N. P. H., et al. 2013, A&A, 555, A72
Long, K. S., Winkler, P. F., & Blair, W. P. 2019, ApJ, 875, 85
Long, K. S., Blair, W. P., Winkler, P. F., & Lacey, C. K. 2020, ApJ, 899, 14
Lotz, J. M., Jonsson, P., Cox, T. J., & Primack, J. R. 2008, MNRAS, 391, 1137
Mateus, A., Sodré, L., Cid Fernandes, R., et al. 2006, MNRAS, 370, 721
Molina, M., Eracleous, M., Barth, A. J., et al. 2018, ApJ, 864, 90
Monreal-Ibero, A., Arribas, S., & Colina, L. 2006, ApJ, 637, 138
Monreal-Ibero, A., Arribas, S., Colina, L., et al. 2010, A&A, 517, A28
Naab, T., & Burkert, A. 2003, ApJ, 597, 893
Oh, S.-H., Staveley-Smith, L., Spekkens, K., Kamphuis, P., & Koribalski, B. S. 2018, MNRAS, 473, 3256
Pilyugin, L. S., & Grebel, E. K. 2016, MNRAS, 457, 3678
Pilyugin, L. S., Grebel, E. K., Zinchenko, I. A., & Kniazev, A. Y. 2014, AJ, 148, 134
Pilyugin, L. S., Grebel, E. K., Zinchenko, I. A., Nefedyev, Y. A., & Vílchez, J. M. 2017, A&A, 608, A127
Pilyugin, L. S., Grebel, E. K., Zinchenko, I. A., et al. 2018, A&A, 613, A1
Pilyugin, L. S., Grebel, E. K., Zinchenko, I. A., Nefedyev, Y. A., & Vílchez, J. M. 2019, A&A, 623, A122
Pilyugin, L. S., Grebel, E. K., Zinchenko, I. A., et al. 2020a, A&A, 639, A96
Pilyugin, L. S., Grebel, E. K., Zinchenko, I. A., et al. 2020b, A&A, 634, A26
Pilyugin, L. S., Zinchenko, I. A., Lara-López, M. A., Nefedyev, Y. A., & Vílchez, J. M. 2021, A&A, 646, A54
Points, S. D., Long, K. S., Winkler, P. F., & Blair, W. P. 2019, ApJ, 887, 66
Relaño, M., Beckman, J. E., Zurita, A., Rozas, M., & Giammanco, C. 2005, A&A, 431, 235
Rich, J. A., Kewley, L. J., & Dopita, M. A. 2014, ApJ, 781, L12
Rich, J. A., Kewley, L. J., & Dopita, M. A. 2015, ApJS, 221, 28
Robertson, B., Bullock, J. S., Cox, T. J., et al. 2006, ApJ, 645, 986
Rodriguez-Gomez, V., Sales, L. V., Genel, S., et al. 2017, MNRAS, 467, 3083
Sakhibov, F., Zinchenko, I. A., Pilyugin, L. S., et al. 2018, MNRAS, 474, 1657
Sarzi, M., Shields, J. C., Schawinski, K., et al. 2010, MNRAS, 402, 2187
Schlafly, E. F., & Finkbeiner, D. P. 2011, ApJ, 737, 103
Singh, R., van de Ven, G., Jahnke, K., et al. 2013, A&A, 558, A43
Springel, V., & Hernquist, L. 2005, ApJ, 622, L9
Stasińska, G., Cid Fernandes, R., Mateus, A., Sodré, L., & Asari, N. V. 2006, MNRAS, 371, 972
Stasińska, G., Vale Asari, N., Cid Fernandes, R., et al. 2008, MNRAS, 391, L29
Stilp, A. M., Dalcanton, J. J., Skillman, E., et al. 2013, ApJ, 773, 88
Storey, P. J., & Zeippen, C. J. 2000, MNRAS, 312, 813
Terlevich, R., & Melnick, J. 1981, MNRAS, 195, 839
Übler, H., Genzel, R., Wisnioski, E., et al. 2019, ApJ, 880, 48
Varidel, M. R., Croom, S. M., Lewis, G. F., et al. 2020, MNRAS, 495, 2265
Walker, I. R., Mihos, J. C., & Hernquist, L. 1996, ApJ, 460, 121
Warner, P. J., Wright, M. C. H., & Baldwin, J. E. 1973, MNRAS, 163, 163
Yan, R., & Blanton, M. R. 2012, ApJ, 747, 61
Zaragoza-Cardiel, J., Beckman, J. E., Font, J., et al. 2015, MNRAS, 451, 1307
Zhou, L., Federrath, C., Yuan, T., et al. 2017, MNRAS, 470, 4573
Zinchenko, I. A., Berczik, P., Grebel, E. K., Pilyugin, L. S., & Just, A. 2015, ApJ, 806, 267
Zinchenko, I. A., Pilyugin, L. S., Grebel, E. K., Sánchez, S. F., & Vílchez, J. M. 2016, MNRAS, 462, 2715
Zinchenko, I. A., Pilyugin, L. S., Sakhibov, F., et al. 2019, A&A, 628, A55

Appendix A: Maps of the properties of galaxies using our measurements

The figures in this section show the properties of galaxies derived from our measurements of the MaNGA spaxel spectra. In each figure, panel a shows the distribution of the surface brightness in the photometric *B*-band across the image of the galaxy in sky coordinates (pixels). North is up and east is left. The pixel scale is 0.5 arcsec. The value of the surface brightness is color-coded. The plus sign (or cross in some cases) shows the kinematic center of the galaxy, the dashed line is the major kinematic axis, the dotted ellipse indicates the optical radius the galaxy. The solid ring marks the position of the spot with the enhanced gas velocity dispersion. The size of the ring corresponds to the point spread function of the MaNGA measurements (2.5 arcsec or 5 pixels). Panel b shows the color-coded observed (line of sight) Hα velocity field of a given galaxy in sky coordinates. Panel c shows the color-coded oxygen abundance map. The oxygen abundances are determined through the *R* calibration from Pilyugin & Grebel (2016). Panel d1 shows the color-coded gas velocity dispersion σ distribution across the image of the galaxy in sky coordinates. Panel d2 shows the gas velocity dispersion as a function of radius for individual spaxels. The BPT type of the spectra is color-coded. Panel e shows the locations of the spaxels with spectra of different BPT types (the AGN-like, H II-region-like, and intermediate) on the image of the galaxy. Panel *f*1 shows the examples of the spaxel spectra in the spot (blue line) and outside the spot (red line). The fluxes in the last spectrum are shifted for the sake of illustration. Panels f2 and f3 show the parts of the spectra from panel f1 around the Hβ (panel f2) and Hα (panel f3) lines.

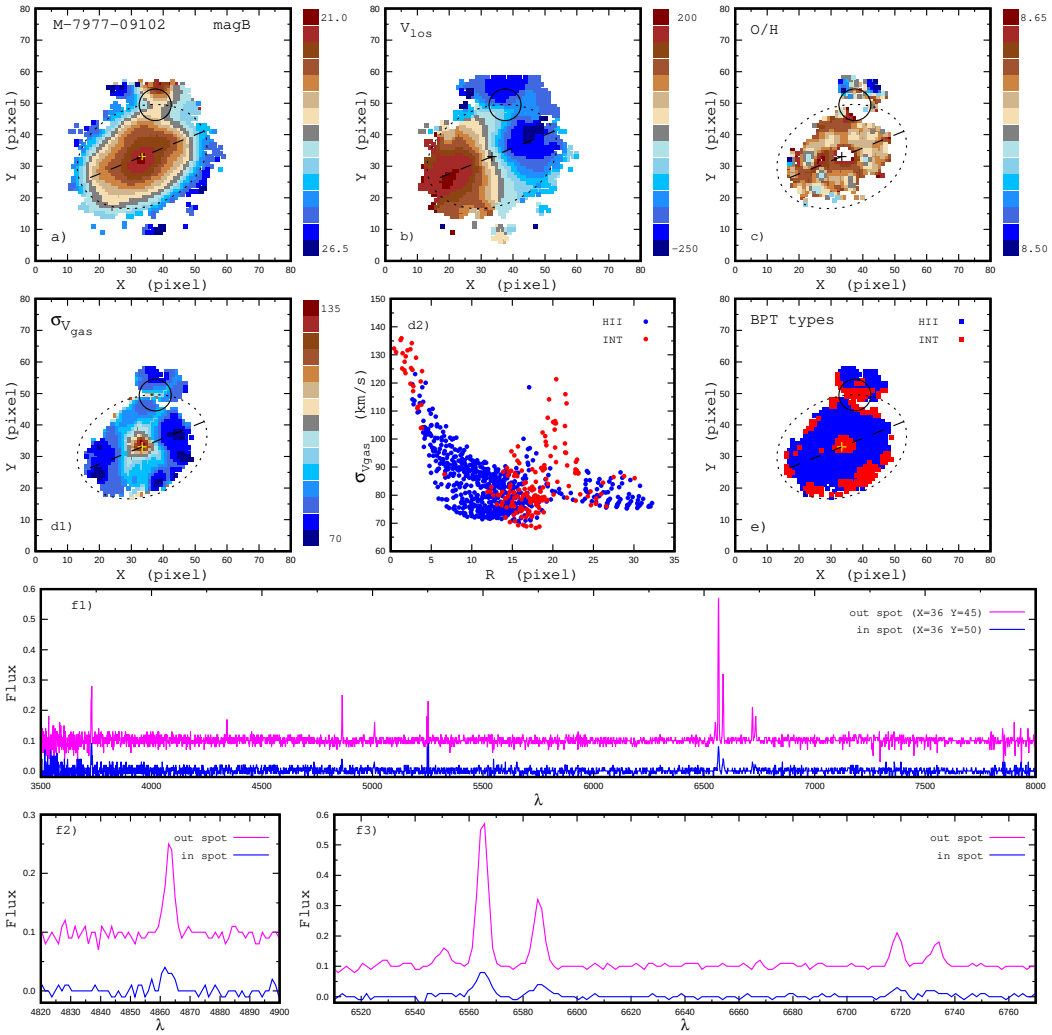

Fig. A.1. Properties of the MaNGA galaxy M-7977-09102. *Panel a*: distribution of the surface brightness in the photometric *B*-band across the image of the galaxy in sky coordinates (pixels). The value of the surface brightness is color-coded. The plus sign (or cross in some cases) shows the kinematic center of the galaxy, the dashed line is the major kinematic axis, the dotted ellipse indicates the optical radius the galaxy. The solid ring marks the position of the spot with the enhanced gas velocity dispersion. The size of the ring corresponds to the point spread function of the MaNGA measurements (2.5 arcsec or 5 pixel). *Panel b*: line-of-sight Hα velocity V_{los} field. *Panel c*: oxygen abundance map. *Panel d1*: gas velocity dispersion σ distribution across the image of the galaxy in sky coordinates. *Panel d2*: gas velocity dispersion as a function of radius for individual spaxels. The BPT type of the spectra is color-coded. *Panel e*: locations of the spaxels with spectra of different BPT types (the AGN-like, H II-region-like, and intermediate) on the image of the galaxy. *Panel f1*: examples of the spaxel spectra in the spot (blue line) and outside the spot (red line). The fluxes in the last spectrum are shifted for the sake of illustration. *Panels f2 and f3*: parts of the spectra from panel f1 around the Hβ (*panel f2*) and Hα (*panel f3*) lines.

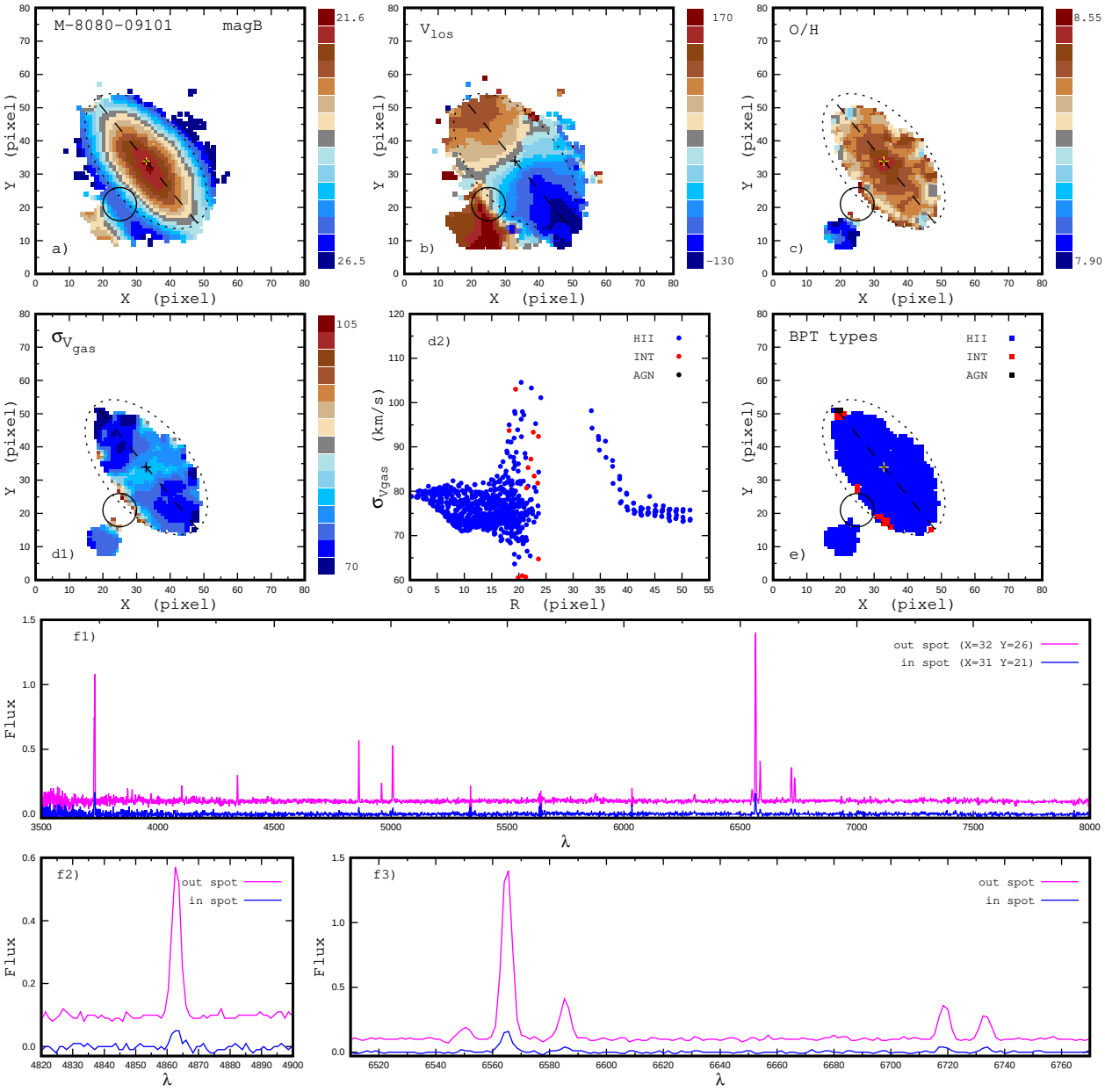

Fig. A.2. Properties of the MaNGA galaxy M-8080-09101. The notation is the same as in Fig. A.1.

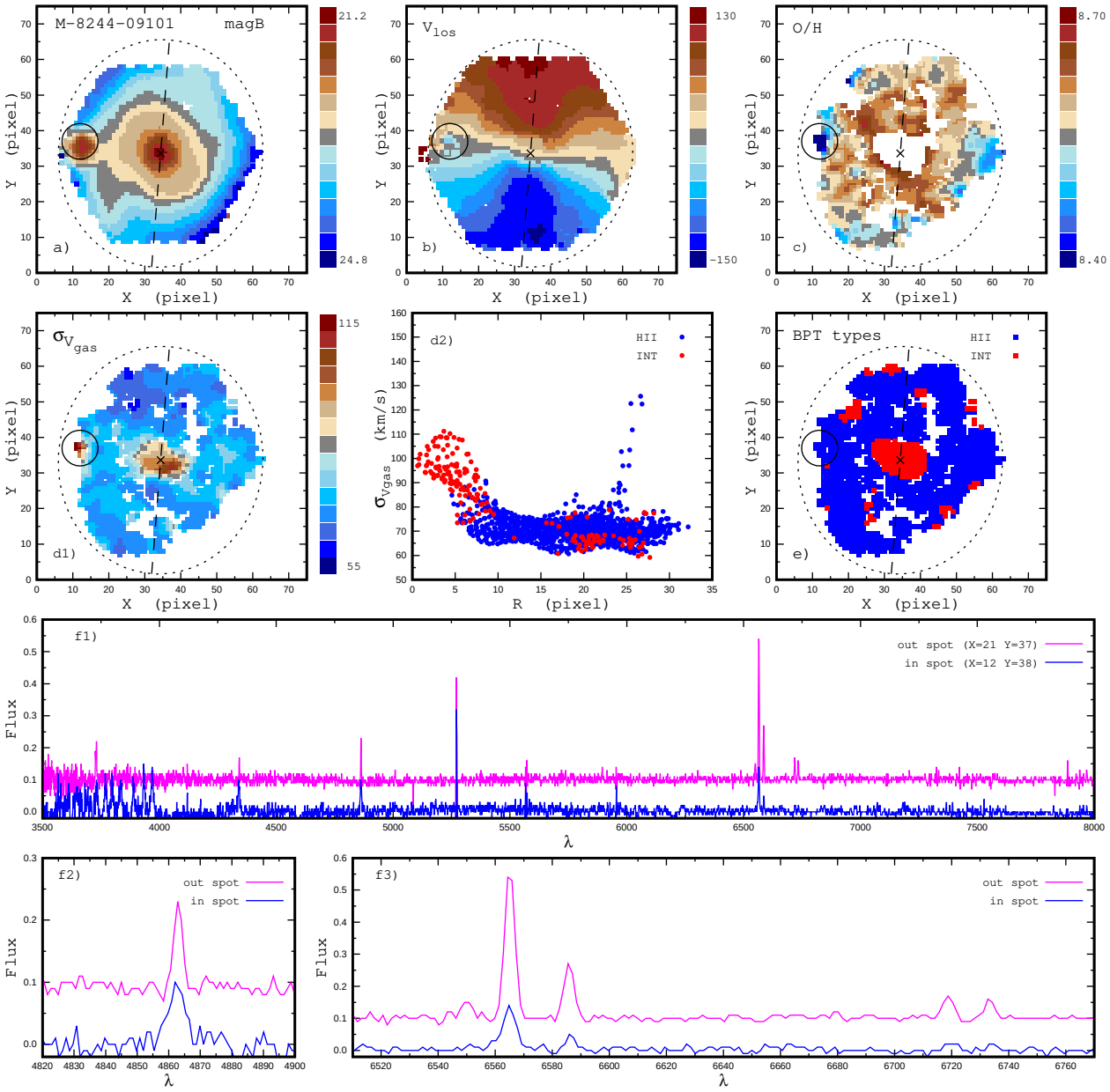

Fig. A.3. Properties of the MaNGA galaxy M-8244-09101 (PGC 025036). The notation is the same as in Fig. A.1.

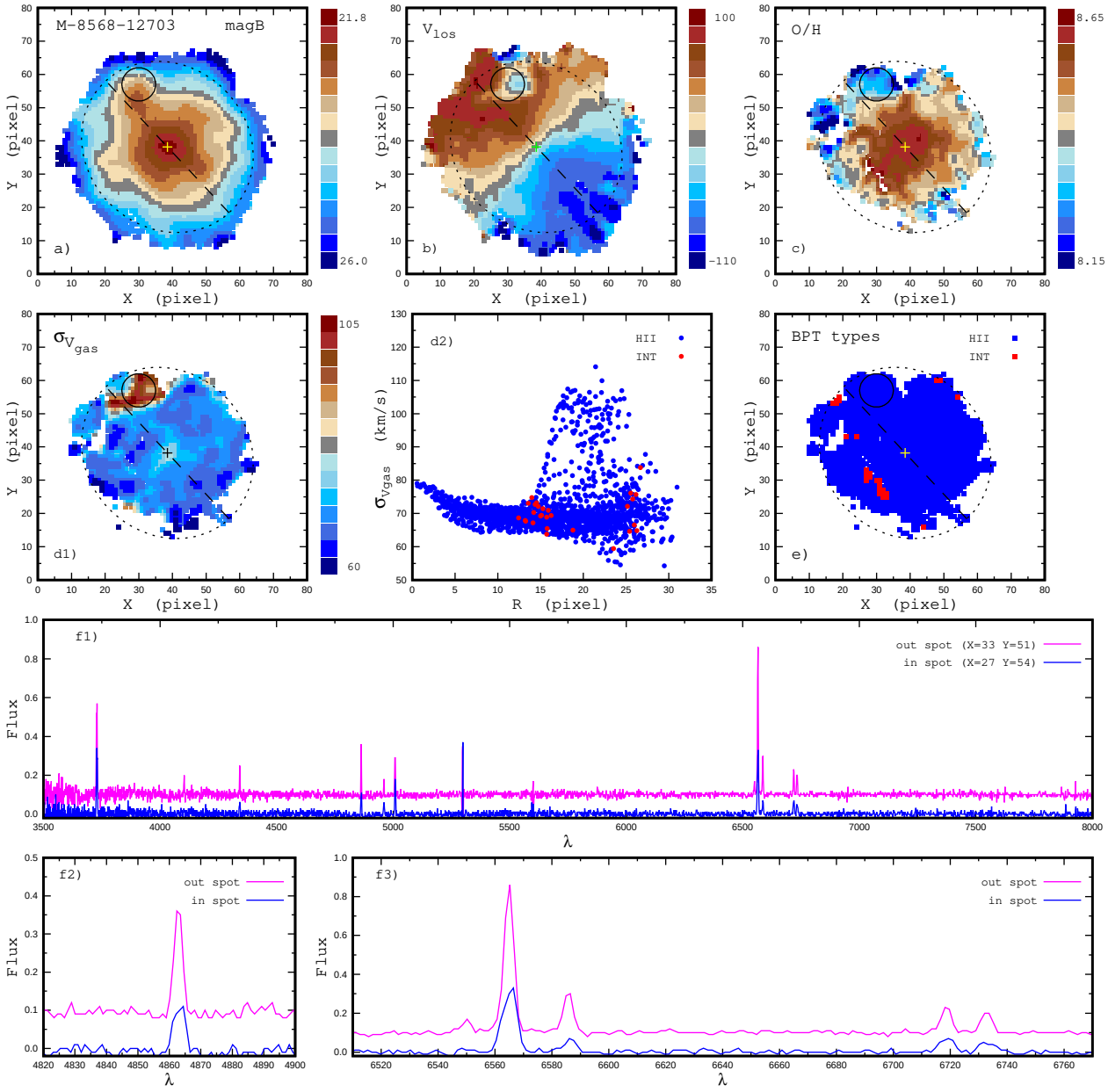

Fig. A.4. Properties of the MaNGA galaxy M-8568-12703. The notation is the same as in Fig. A.1.

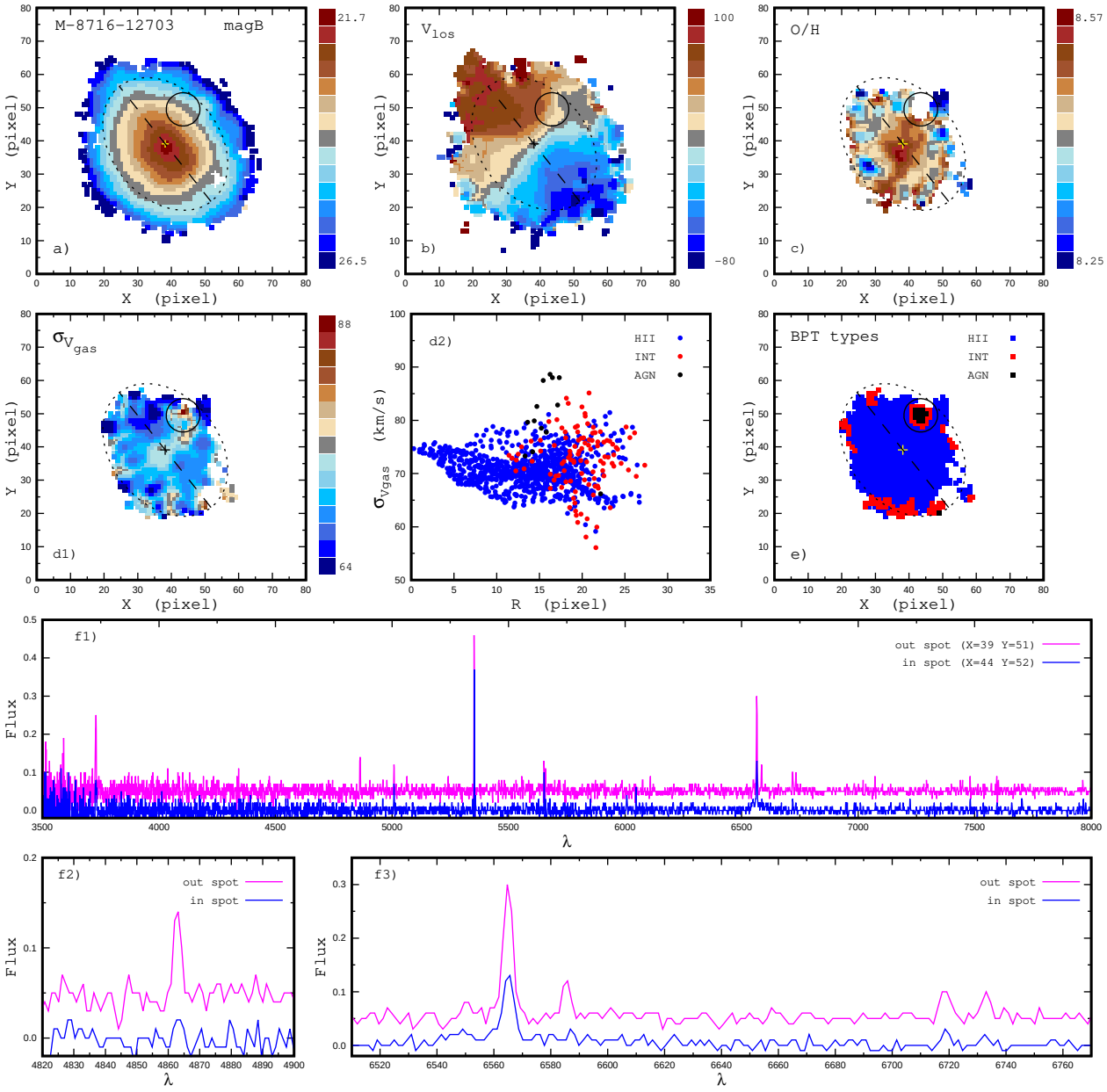

Fig. A.5. Properties of the MaNGA galaxy M-8716-12703. The notation is the same as in Fig. A.1.

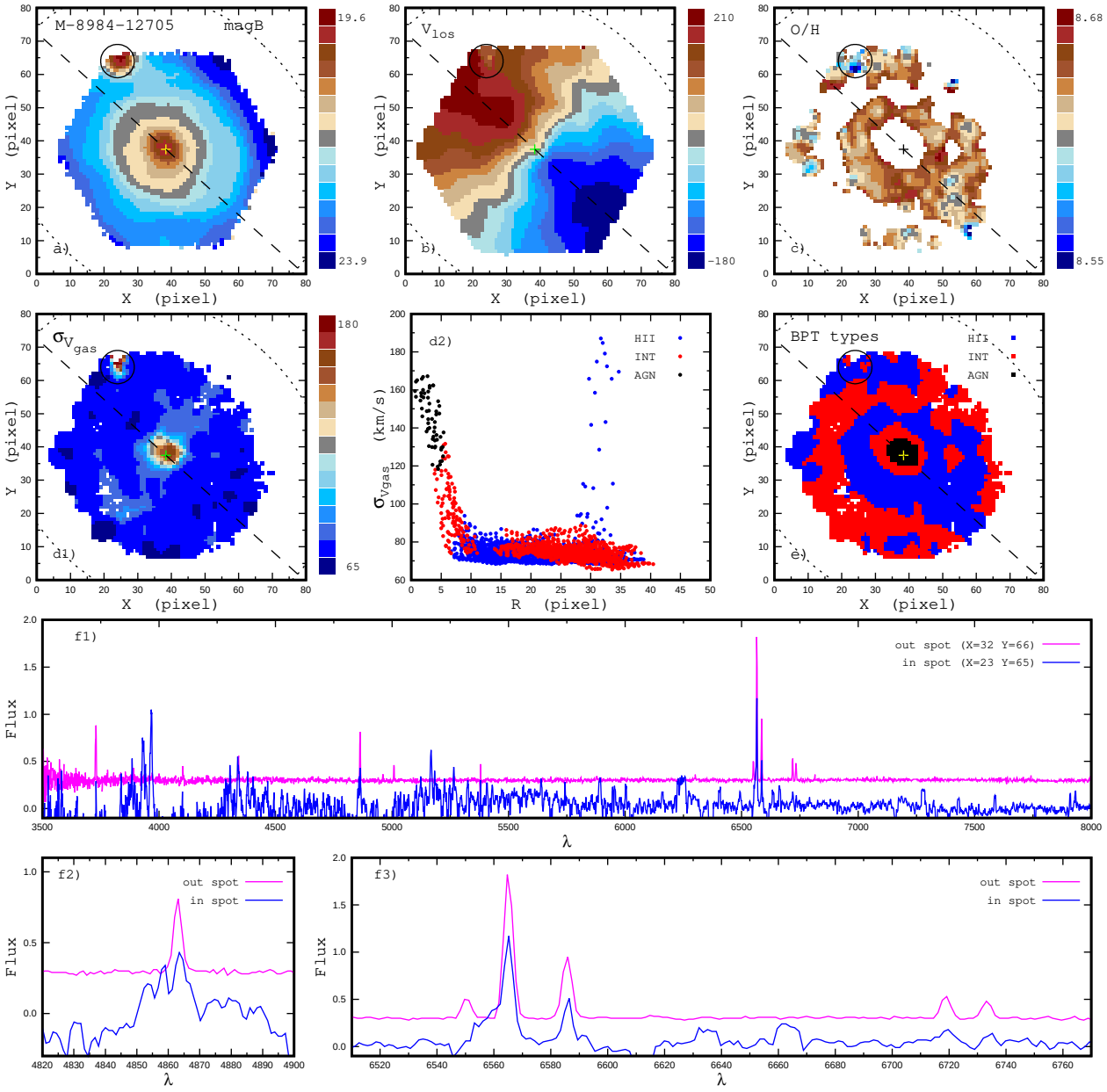

Fig. A.6. Properties of the MaNGA galaxy M-8984-12705 (NGC 5251). The notation is the same as in Fig. A.1.

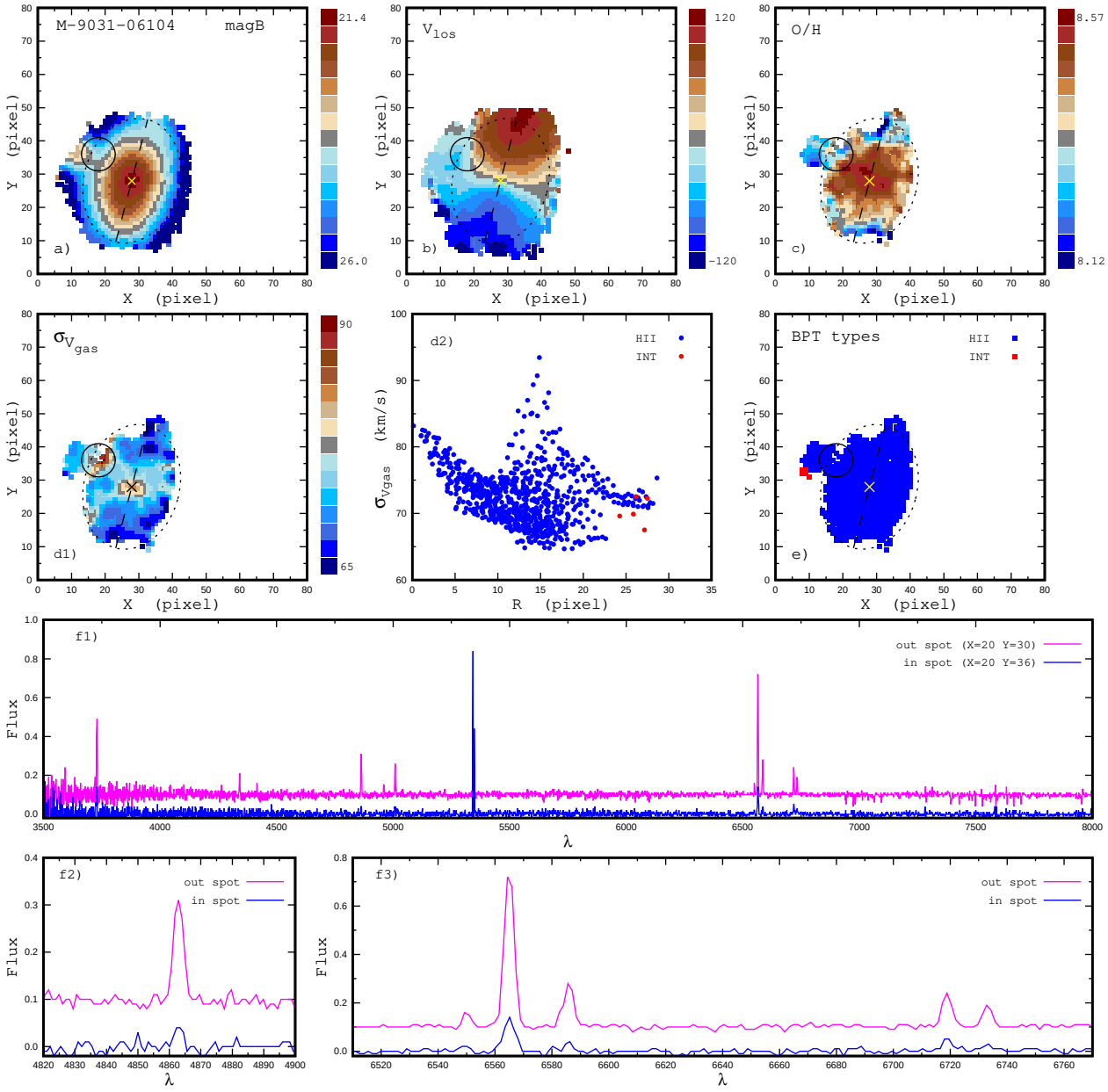

Fig. A.7. Properties of the MaNGA galaxy M-9031-06104. The notation is the same as in Fig. A.1.

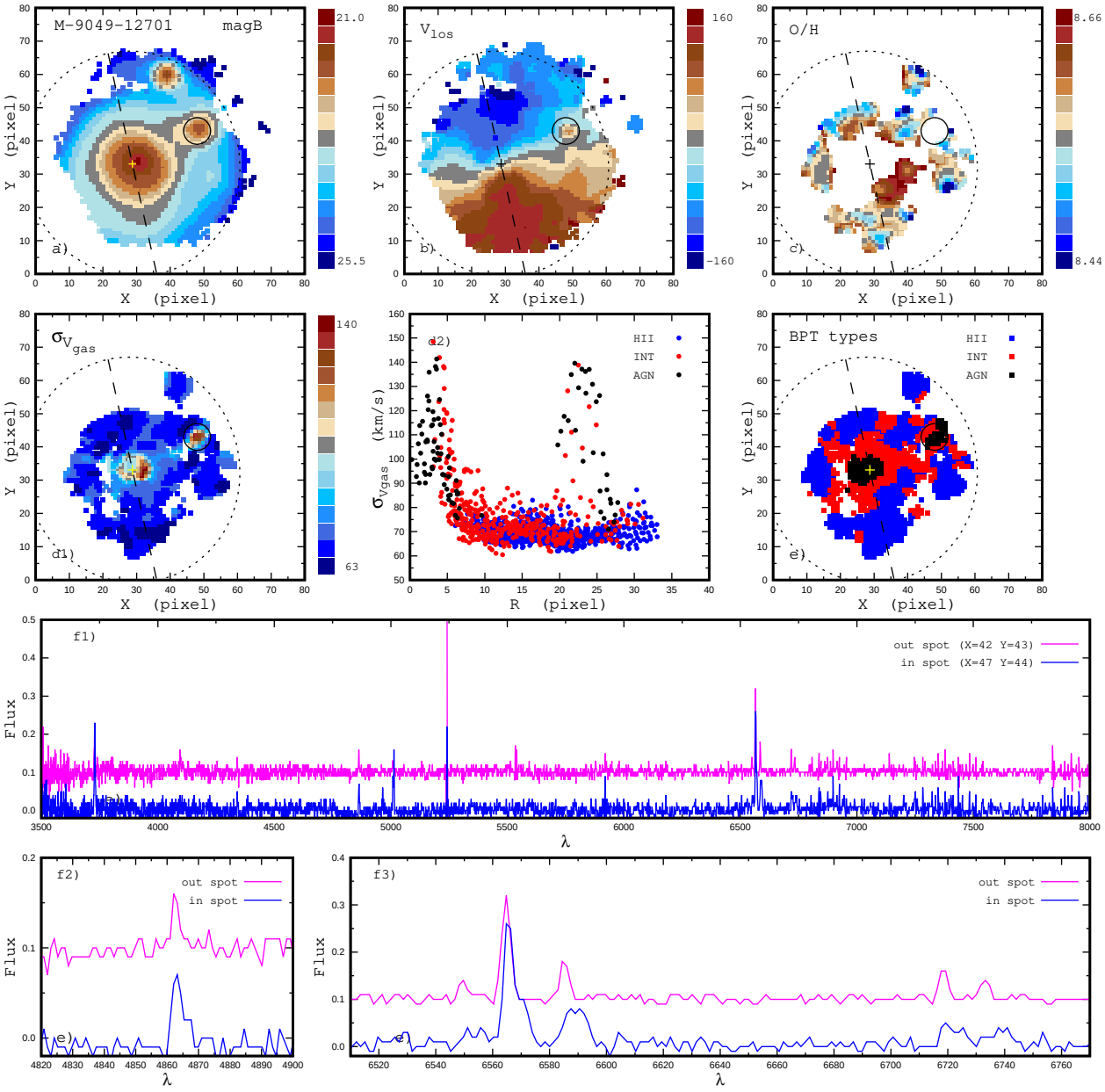

Fig. A.8. Properties of the MaNGA galaxy M-9049-12701 with double-peaked emission lines in the spot of the enhanced gas velocity dispersion. The notation is the same as in Fig. A.1.

Appendix B: Maps of the properties of galaxies for the MaNGA data analysis pipeline (DAP) measurements

The figures in this section show the same as the figures in the previous section but the properties of galaxies are derived from the DAP measurements.

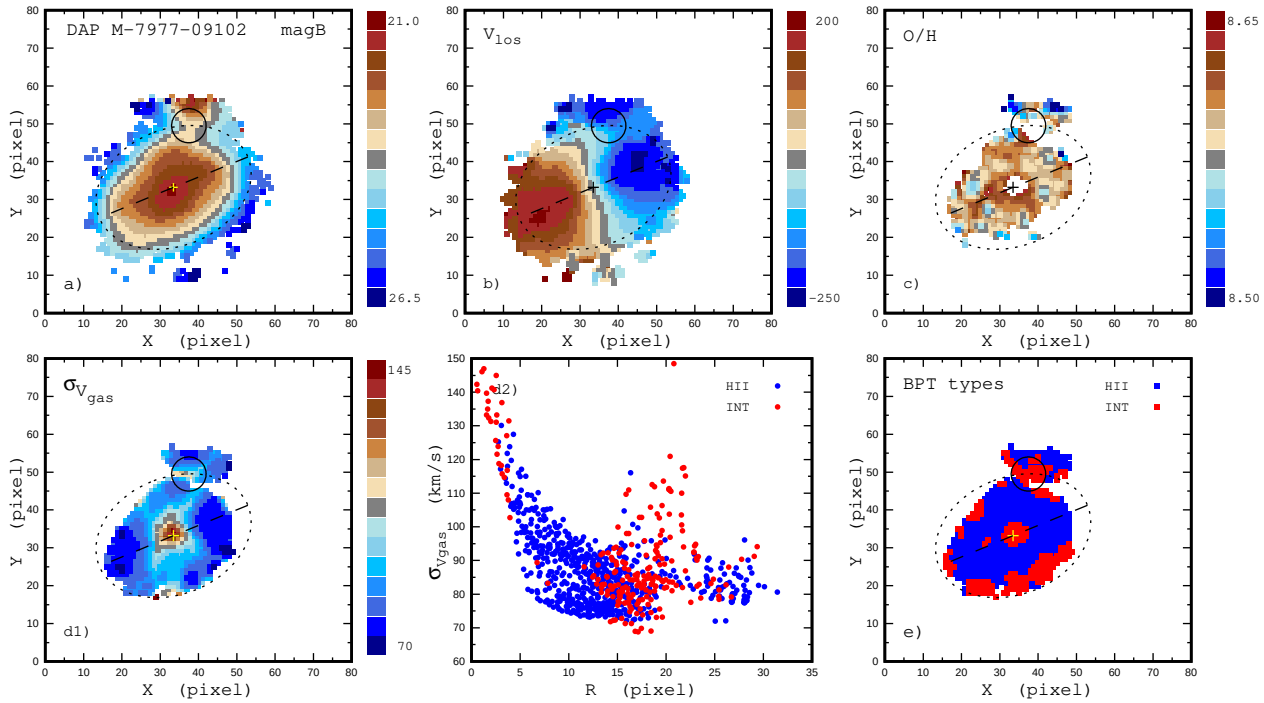

Fig. B.1. Properties of the MaNGA galaxy M-7977-09102 for the DAP measurements. *Panel a*: distribution of the surface brightness in the photometric *B*-band across the image of the galaxy in sky coordinates (pixels). The value of the surface brightness is color-coded. The plus sign (or cross in some cases) shows the kinematic center of the galaxy, the dashed line is the major kinematic axis, the dotted ellipse indicates the optical radius the galaxy. The solid ring marks the position of the spot with the enhanced gas velocity dispersion. The size of the ring corresponds to the point spread function of the MaNGA measurements (2.5 arcsec or 5 pixel). *Panel b*: line-of-sight Hα velocity $V_{\rm los}$ field. *Panel c*: oxygen abundance map. *Panel d1*: gas velocity dispersion σ distribution across the image of the galaxy in sky coordinates. *Panel d2*: gas velocity dispersion as a function of radius for individual spaxels. The BPT type of the spectra is color-coded. *Panel e*: locations of the spaxels with spectra of different BPT types (the AGN-like, H II-region-like, and intermediate) on the image of the galaxy.

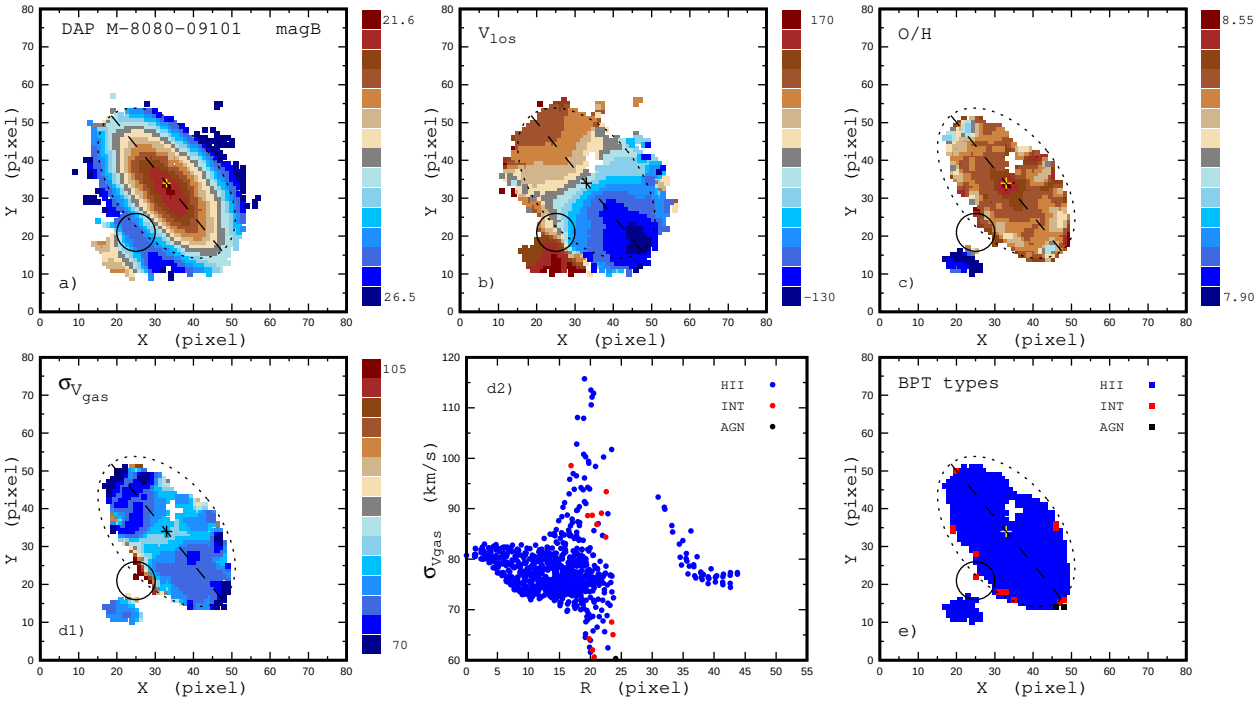

Fig. B.2. Properties of the MaNGA galaxy M-8080-09101 for the DAP measurements. The notation is the same as in Fig. B.1.

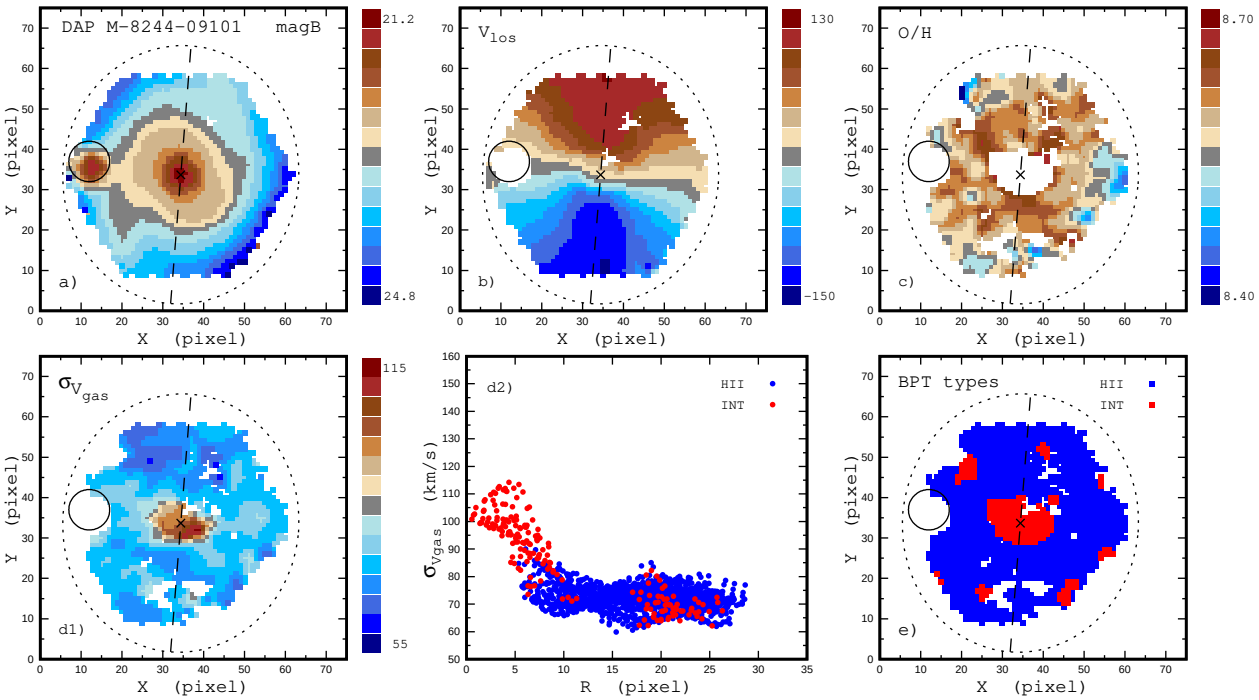

Fig. B.3. Properties of the MaNGA galaxy M-8244-09101 (PGC 025036) for the DAP measurements. The notation is the same as in Fig. B.1.

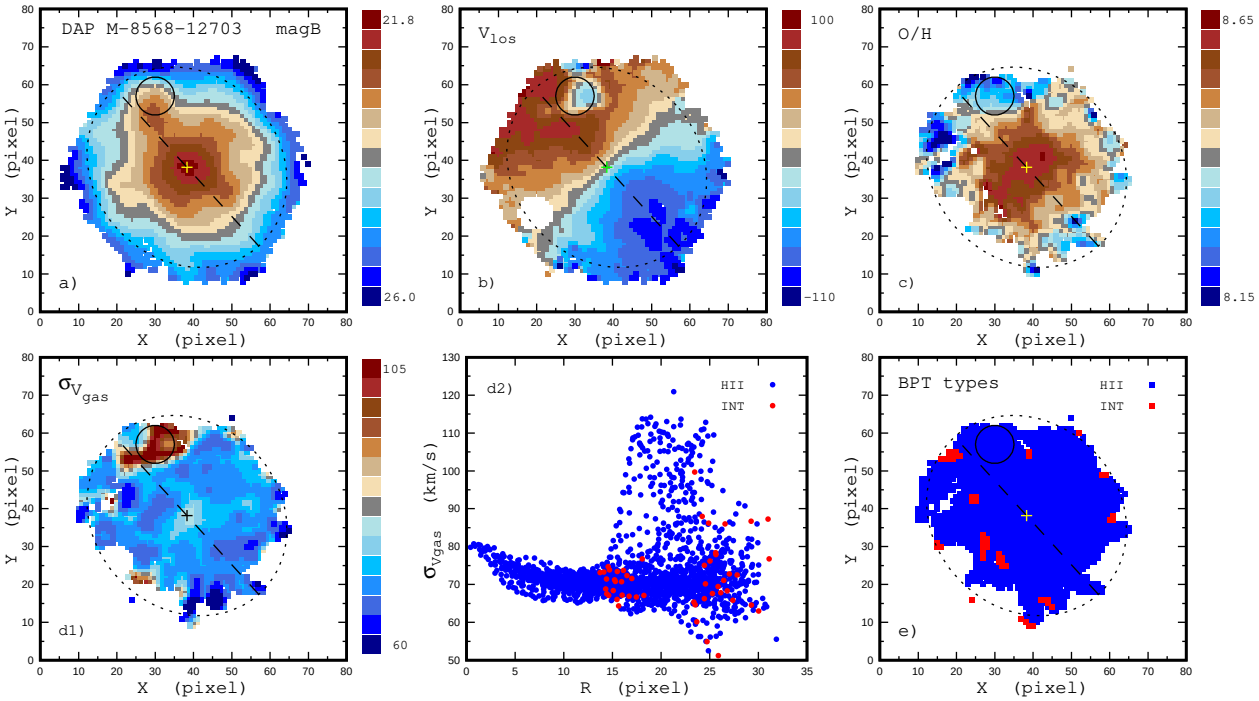

Fig. B.4. Properties of the MaNGA galaxy M-8568-12703 for the DAP measurements. The notation is the same as in Fig. B.1.

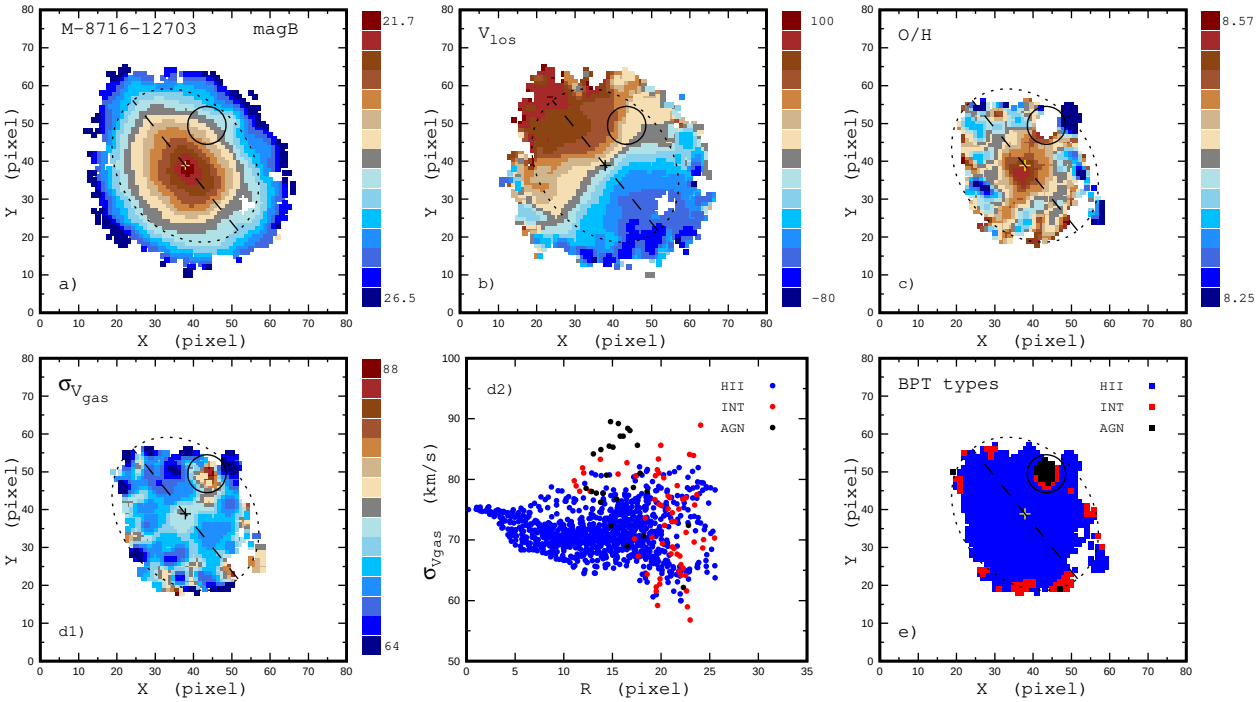

Fig. B.5. Properties of the MaNGA galaxy M-8716-12703 for the DAP measurements. The notation is the same as in Fig. B.1.

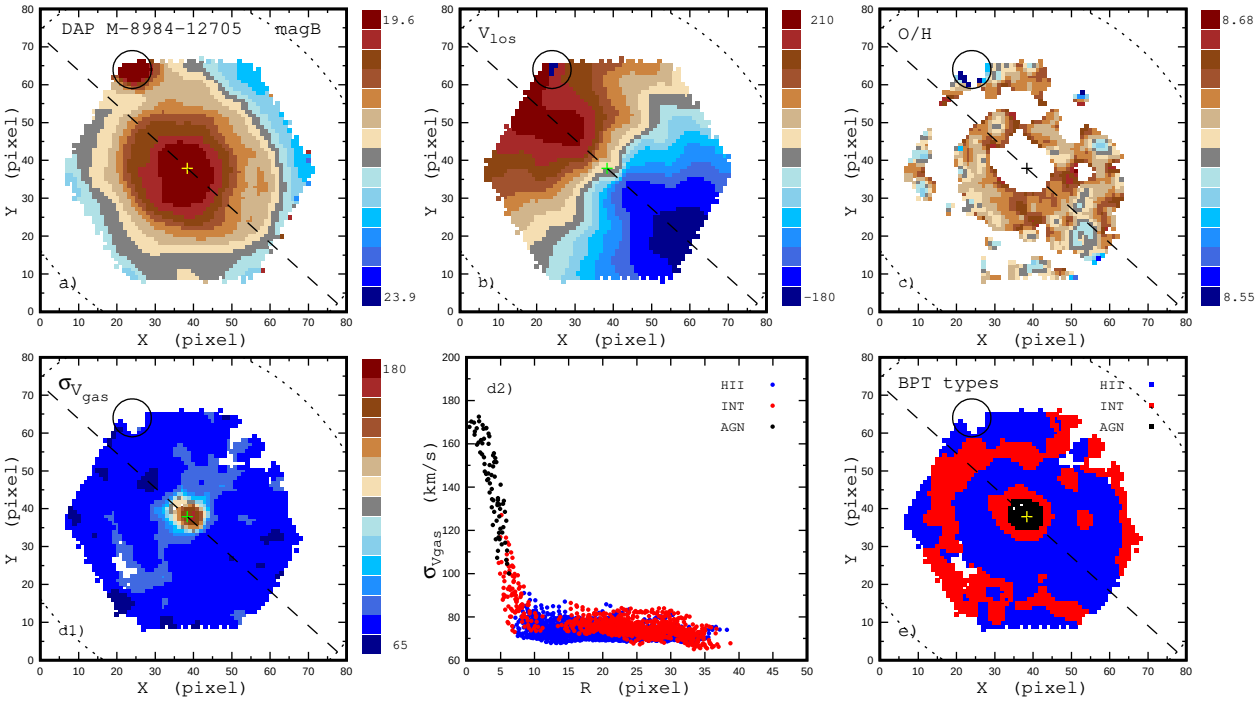

Fig. B.6. Properties of the MaNGA galaxy M-8984-12705 (NGC 5251) for the DAP measurements. The notation is the same as in Fig. B.1.

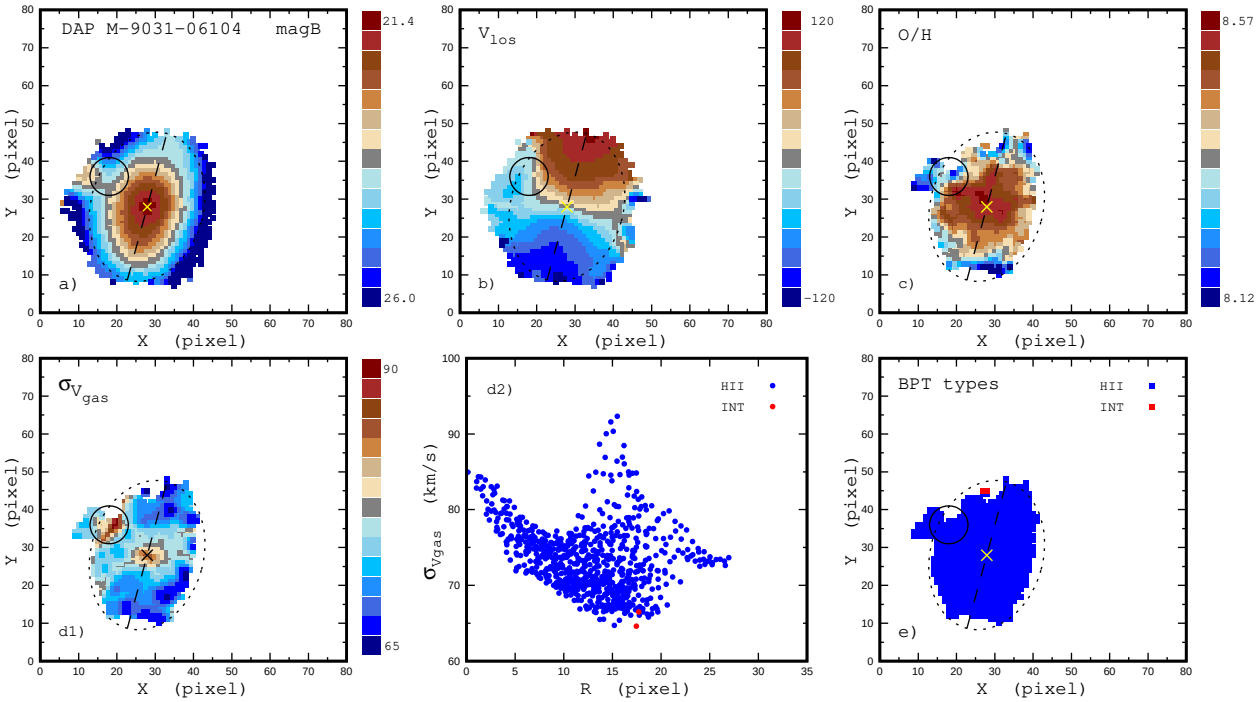

Fig. B.7. Properties of the MaNGA galaxy M-9031-06104 for the DAP measurements. The notation is the same as in Fig. B.1.